

Critical Flux of Ultrathin Silicon Membranes in Tangential Flow Filtration of Protein Solutions

S. Danial Ahmad

Submitted in Partial Fulfillment of the
Requirements for the Degree
Master of Science

Supervised by
Professor James McGrath

Department of Biomedical Engineering
Arts, Sciences and Engineering
Edmund A. Hajim School of Engineering and Applied Sciences

University of Rochester

Rochester, New York

2019

To former President Barack Obama.

Biographical Sketch

The author was born in the city of Karachi in Pakistan on October 19th, 1994. He moved to the United States when he was two years old and was raised in Henrietta, NY. After graduating high school he attended the State University of New York (SUNY) at Geneseo where he graduated with two Bachelor of Arts degrees in Physics and Mathematics. At SUNY Geneseo he was an undergrad research assistant who conducted research with the Department of Physics and Astronomy. There, his work focused on classifying extragalactic star clusters through ultraviolet image analysis under the direction of Dr. Anne Pellerin. One year after graduating from SUNY Geneseo in 2016, the author began a Master's degree in Biomedical Engineering at University of Rochester in 2017. There, he focused on researching ultrathin silicon nanomembranes in tangential flow filtration with guidance from Dr. James McGrath. His work was presented in both the Center for Emerging & Innovative Sciences annual meeting in 2019 and the North American Membrane Society annual meeting in 2019.

The author has the following publication from SUNY Geneseo:

Messa, M., Adamo, A., Östlin, G., Calzetti, D., Grasha, K., Grebel, E.K., Shabani, F., Chandar, R., Dale, D.A., Dobbs, C.L., Elmegreen, B.G., Fumagalli, M., Gouliermis, D.A., Kim, H., Smith, L.J., Thilker, D.A., Tosi, M., Ubeda, L., Walterbos, R., Whitmore, B.C., Fedorenko, K., Mahadevan, S., Andrews, J.E., Bright, S.N., Cook, D.O., Kahre, L., Nair, P., Pellerin, A., Ryon, J.E., **Ahmad, S.D.**, Beale, L.P., Brown, K., Clarkson, D.A., Guidarelli, G.C., Parziale, R., Turner, J., Weber, M. *The young star cluster population of M51 with LEGUS – I. A comprehensive study of cluster formation and evolution. Monthly Notices of the Royal Astronomical Society.* 2017;473(1):996–1018.

The author is currently writing a manuscript in conjunction with another member of McGrath Lab (Kilean Lucas) based on their combined work.

Acknowledgments

First and foremost I would like to thank my advisor Dr. James McGrath for everything he's done to help me succeed. I truly appreciate his guidance and patience when addressing my questions and concerns. Through all the time we've spent in meetings and through numerous emails, he's shown me immeasurable mentorship and I'm thankful for his support. I would also like to extend gratitude to Dr. Mark Buckley and Dr. Paul Funkenbusch for agreeing to be members of my committee. Their time is valuable and I appreciate every minute they have spent working with me.

Next, I would like to thank the members and affiliates of my lab for helping me with experiments, providing scientific insights, and quality jokes. Kilean Lucas helped me throughout the course of my thesis with all experimental and theoretical nuances, so I would principally like to thank him first. I would also like to thank Mehdi Dehghani for supplying the track etched microfluidic devices I used for this research and for helping me use them in experiments. For entertaining my questions about data analysis, microscopy, and scientific nuances, as well as for their interesting senses of humor, I would like to thank Kayli Hill, Tejas Khire,

Alec Salminen, Luis Delgadillo, Dr. Jonathon Flax, and Dr. Greg Madejski. Your thoughts were invaluable and I appreciate the perspective you all provided. Lastly, I'd like to thank Molly McCloskey, Raquel Ajalik, and Mike Klaczko for their support and encouragement.

Amongst my peers I'd specifically like to thank Dr. Alex Kotelsky from Buckley Lab for sharing his passion for research and teaching. His mentorship in my first year here was invaluable and helped inspire some of my academic choices. I would also like to thank my close friend and current UR medical student Hussain Bawany for his support, friendship, and willingness to go to weekly yoga sessions with me. Thank you also to the BME administrative staff, specifically Donna Porcelli, Ania Dworzanski, and Judy Principe, for entertaining all my questions about the program.

Finally, I'd like to express gratitude to my friends and family for their unwavering support and kindness. There's far too many names to list but you all make Rochester a nicer place to be in.

Abstract

Dead-end filtration of protein-rich fluids through ultrathin nanomembranes (< 100 nm thick freestanding) leads to rapid surface fouling due to their high permeability and lack of internal structure. By contrast, tangential flow operations with ultrathin membranes and complex biofluids (such as hemodialysis) have been found to proceed for days without a loss of membrane permeability, even in the presence of some ultrafiltration. Inspired by these observations, here we systematically test the hypothesis that ultrathin nanoporous membranes exhibit a higher "critical flux" in tangential flow filtration (TFF) than conventionally thick membranes. After removing protein aggregates by centrifugation, we show that solutions of bovine serum albumin (BSA) as concentrated as 10 mg/ml achieve a critical flux of 1157 LMH (l/m^2 h) in a microfluidic device featuring 18.8% porosity nanoporous silicon nitride (NPN) membranes. This critical flux is approximately five times higher than literature values achieved for TFF microfiltration, where a flux of 220 LMH was acquired with 0.2 μ m track-etched (TE) membranes using 1 mg/ml BSA. Repeating our studies with 10 μ m thick TE membranes with the same size (\sim 50 nm diameter) and number (\sim 5 x 10⁷) of pores as NPN confirms our hypothesis

that membrane thinness leads to a higher critical flux. Based on the fact that transmembrane pressures (TMP) in these studies are higher for TE vs. NPN with the same ultrafiltration rate we posit a mechanism for critical flux enhancement: the inherent thinness of NPN mitigates the formation of a stagnant protein ‘cake layer’ on the membrane surface and instead promotes a ‘flowing protein cake’. More specifically, a lower TMP limits the fouling experienced by NPN versus TE membranes and this confers long term viability and performance. To further our understanding of membrane fouling we then expand our study by exploring membrane capacity. We define capacity as the number of particles on a membrane surface before a significant rise in TMP occurs due to a decrease in permeability. By experimentally testing slit pore and high porosity circle pore ultrathin microporous membranes in dead-end filtration of polystyrene bead solutions, we find that these membranes have capacities of ~60% and ~80% respectively.

Contributions and Funding Sources

This research was supervised by a thesis committee consisting of Professor James McGrath and Professor Mark Buckley of the Department of Biomedical Engineering as well as Professor Paul Funkenbusch of the Department of Mechanical Engineering.

Electron microscopy images of the ultrathin nanoporous membranes in Chapter 2 were provided by Dr. Greg Madejski (McGrath Lab, University of Rochester). The gold particle capture experiments (with images) performed in Chapter 2 were done in conjunction with Kilean Lucas (McGrath Lab, University of Rochester). The COMSOL modeling and images used in Chapter 2 were also provided by Kilean Lucas (McGrath Lab, University of Rochester). Lastly, the track etched membrane devices and track etched membrane imagery were provided by Mehdi Dehghani (Gaborski Lab, Rochester Institute of Technology).

All other work conducted for this thesis was done independently by the author. This work was funded by the United States Department of Defense (DoD Award #W81XWH-18-1-0560) and the Center for Integrated Research and Computing (CEIS Award #1830C001).

Contents

Biographical Sketch	iii
Acknowledgments	v
Abstract	vii
Contributions and Funding Sources	ix
List of Tables	xiv
List of Figures	xxii
1 Introduction	1
1.1 Silicon Nanomembrane Technology in Microfluidic Devices	1
1.2 Extracellular Vesicles and Cancer Biomarkers	4
1.3 Tangential Flow Filtration, Critical Flux, and Fouling	6
1.4 Filtering Biologics and Virus Purification	9
1.5 Microplastic Contamination in the Environment and its Physiological Implications	11
1.6 Thesis Outline and Research objectives	12

2	Critical Flux of Nanoporous Membranes in Tangential Flow Filtration	15
2.1	Introduction	15
2.2	Materials and Methods	16
2.2.1	Nanoporous Membrane Device Manufacture	16
2.2.2	Silicon Gasket Processing	17
2.2.3	Poly-dimethylsiloxane Preparation	18
2.2.4	Nanoporous Membranes	19
2.2.5	UV Ozone Bonding	19
2.2.6	Track Etched Membrane Device Manufacture	20
2.2.7	Protein Serum Preparation	21
2.2.8	NPN Microfluidic Device Overview	25
2.2.9	Microfluidic System	25
2.2.10	Experimental Process and Data Collection	27
2.2.11	Membrane Chip Analysis and Statistics	28
2.2.12	Nanoparticle Sample Preparation	28
2.2.13	Definition of Critical Flux and Mathematical Methods	29
2.3	Results	29
2.3.1	Optimizing Critical Flux in Nanoporous Systems	29
2.3.2	Effect of Varying Protein Concentration and Supply Flow Rate	32
2.3.3	Comparing NPN performance to Track-Etched Membranes	35
2.3.4	Critical Flux Experiments with Gold Particle Capture	39
2.4	Discussion	45

2.4.1	Protein Pre-filtration, Membrane Porosity, and Critical Flux Performance	45
2.4.2	The Relationship Between Porosity and Pore Morphology	46
2.4.3	Parameter Sweep and NPN versus Track-Etched Membrane Performance	49
2.4.4	Gold Nanoparticle Capture and Critical Flux	51
3	Capacity of Microporous Membranes with Microparticle Contamination	53
3.1	Introduction	53
3.2	Materials and Methods	55
3.2.1	Microporous Membrane Device Manufacture	55
3.2.2	Extended Length Membrane Device Fabrication	56
3.2.3	Mathematical Modeling of Microporous Membrane Systems	56
3.2.4	Polystyrene Bead Sample Preparation	61
3.2.5	Experimental Process and Data Collection	62
3.2.6	Video Recording of Capacity Experiments	62
3.2.7	Membrane Chip Analysis and Statistics	63
3.2.8	Definition of Capacity	64
3.3	Results	65
3.3.1	Mathematical Modeling of $8\mu\text{m}$ Membranes	65
3.3.2	Experimental Results with $8\mu\text{m}$ Slit Membranes	66
3.3.3	Experimental Results with $3\mu\text{m}$ Circle Pore Membranes .	73

3.4	Discussion	75
3.4.1	Mathematical Modeling of Microporous Membrane Systems	75
3.4.2	Differences in Model and Experimental Results	77
3.4.3	Analytical Tools for Microplastics Analysis	78
3.4.4	Membranes as Sensors for Bioprocessing	79
4	Summary and Future Directions	80
4.1	Summary	80
4.1.1	Optimizing Critical Flux of Ultrathin NPN	80
4.1.2	Comparing NPN and TE Critical Flux	82
4.1.3	Gold Particle Capture	83
4.1.4	Mathematical Modeling of 8 μm Slit Membrane Capacity	84
4.1.5	8 μm Slit Membrane and 3 μm Circle Pore Experimental Results	85
4.2	Future Directions	85
4.2.1	Analyzing Biofluids in TFF	85
4.2.2	Assessment of Functionalized Membrane Surfaces	86
	Bibliography	87

List of Tables

- 3.1 An overview of all experiments performed in this chapter. Each experiment was run in triplicate. 63
- 3.2 Information relating to capacity of membranes is depicted in this table. The row "Max Beads" is the definition of 100% occupancy. Membranes are capable of supporting an occupancy well beyond that number and can even remain permeable with robust bead cake formations on them. 65

List of Figures

- 1.1 A top view of a typical microfluidic device setup featuring an ultrathin silicon nanomembrane chip. The glass slide is 40 mm long and supports the device. The chip featured in this particular device is 2.7% porosity with an average pore diameter of 33.2 nm. 2

-
- 1.2 A diagram depicting common contents of exosomes adapted from Rajagopal and Harikumar (2018). Nucleic acid assessment, particularly of miRNAs, is a commonly discussed approach to exosome analysis for early cancer detection [10]. 5
- 1.3 Dead end filtration (1.3A) can result in the buildup of protein cakes as thick as 8 μm while tangential flow filtration (1.3B) can result in no protein deposition at all. In 1.3A a protein solution at 60 mg/ml was normally flown onto a membrane surface, depositing large amounts of protein in a cake. In 1.3B, protein laced with gold nanoparticles was tangentially flown across the surface of the membrane, leaving no trace of protein behind with only particles on the surface. Imaged by Kilean Lucas (University of Rochester) 7
- 1.4 TFF with specific flow modes allows for movement of protein through a membrane without cake formation while simultaneously capturing particles in solution. This capture capability is the basis of the "Tangential Flow for Analyte Capture" model currently being developed [3]. 8

-
- 1.5 In TFF the formation of protein cake layers is facilitated by driving protein towards a membrane surface with higher TMPs enhancing this process. Thicker membranes will experience higher TMPs due to higher resistance to transmembrane flow, thus this research posits that ultrathin membranes will promote the formation of flowing protein cake layers due to lower TMPs and this will increase critical flux. 9
- 2.1 A layer diagram of the nanoporous device design featured in this research. A glass slide on the bottom provides rigid support for the gasket layers above it and the PDMS capstone layer provides support for syringe tips. In the middle of the device a membrane can be seen. The gasket layers create two fluid channels that are separated by this membrane. 17
- 2.2 Vector image diagram of an NPN microfluidic device with a flow pattern for tangential flow filtration. 21
- 2.3 Vector image diagram of a TE microfluidic device with a flow pattern for tangential flow filtration. Note in this device there are inlets and outlets on both sides of the device with ultrafiltration occurring through a membrane sheet in a confined area. 22
- 2.4 A standard curve for BSA suspended in PBS. This was measured by using weighed samples of BSA and used as a point of reference for assessing concentration of processed BSA serum. 23

-
- 2.5 1mg/ml BSA suspended in PBS from multiple samples was aliquoted and measured for protein concentration post centrifugation. The concentration of each sample is still 1 mg/ml, indicating no change in concentration due to centrifugation. 24
- 2.6 DLS analysis of pre and post centrifuged BSA samples lacks enough evidence to suggest a reduction in average particle diameter given that $p > 0.05$ in a paired t-test. The presence of aggregates is later verified through the pressure data in experiments. 25
- 2.7 A device diagram indicating flow and sensor orientation for all experiments. The bottom inlet (left side) is closed off while the top inlet receives fluid from a syringe pump. Fluid is pulled through the membrane and bottom outlet by another syringe pump. 26
- 2.8 Pressure data detailing the effect of centrifugation of BSA samples on critical flux. Experiments performed on a 2.7% porosity membrane show stable transmembrane pressure regimes post centrifugation that are comparable to control experiments. 30
- 2.9 Pressure data detailing the effect of porosity on critical flux. Experiments were performed on a 2.7% porosity membrane and an 18.8% porosity membrane. Higher porosity allows the system to achieve better performance in the form of a lower TMP. 31
- 2.10 Critical flux results for NPN of varying porosities. Higher porosity membranes elucidated higher performance with respect to centrifuged 1mg/ml BSA suspended in PBS. 32

- 2.11 Critical flux results for varying BSA concentrations between 1mg/ml and 60mg/ml incident upon an 18.8% porosity membrane. Dead end filtration was possible up to BSA concentrations of 10mg/ml, while at 30mg/ml and 60mg/ml critical flux ratios dropped off accordingly. 34
- 2.12 Critical flux results for varying supply rate Q_s for the purpose of preventing protein cake formations on the top surface of the membrane. Note that critical flux in this case isn't represented by a ratio rather a specific value. Small increases in supply rate provided slightly improved critical flux rates however there are diminishing returns at higher supply rates. Overall critical flux ratio decreases, however, signifying the advantage of using a slower supply rate. 35
- 2.13 Critical flux results for varying BSA concentration with both track etched membranes and NPN results. Track etched membranes have significantly lowered performance across the board. Note that 30mg/ml BSA on NPN and 1mg/ml BSA on Track Etched membranes offer similar performance with respect to critical flux ratio. 37
- 2.14 Critical flux results for varying supply rate Q_s on both NPN and track etched membranes. 38
- 2.15 Stable pressure data for a critical flux of $15\mu\text{l}/\text{min}$. NPN based systems exhibit robust performance with lower transmembrane pressures than track etched systems at similar protein concentrations. 39

-
- 2.16 Stable pressure data for two critical flux values ($3\mu\text{l}/\text{min}$ and $6\mu\text{l}/\text{min}$). Even with thirty times more BSA in solution, NPN based systems exhibit still outperform their track etched counterparts with a lower transmembrane pressure. 40
- 2.17 Initial transmembrane pressure values for the varied supply rate experiments featuring NPN and track etched membranes. The NPN data comes from experiments conducted with $30\text{mg}/\text{ml}$ BSA in PBS and the track etched data includes $1\text{mg}/\text{ml}$ BSA in PBS. Increasing supply rates resulted in negligible TMP changes in NPN while track etched systems experienced rapid increases in TMP. . . 41
- 2.18 Critical flux experimental data for particle laced biofluid experiments. The NPN featured in this research has 10^7 pores available so the first set of experiments matched this number for nanoparticle concentration. Both single and mixed particles were capable of achieving critical flux at this concentration, however increasing concentration by an order of magnitude resulted in an inability to attain critical flux for mixed particle experiments. 42
- 2.19 Critical flux experimental data for particle laced biofluid experiments at a concentration of 10^9 particles. 30nm particles passed through the membrane without incident while 60nm and $60/100\text{nm}$ mixed particle experiments had poor critical flux performance in comparison. 43

2.20	TEM imagery of NPN after an experiment with 10^7 gold nanoparticles suspended in 1mg/ml BSA in PBS incident upon its surface. A capture efficiency of 80% is shown here with no visible protein cake formation.	44
2.21	Low Porosity (2.7%)	47
2.22	High Porosity (18.8%)	47
2.23	Geometric constructs in low porosity membranes such as "divots" and large pore orifices play an integral role in the reduced performance of these membranes. Higher porosity membranes have fully constructed pores with a slightly tapered geometry, improving their function overall.	47
2.24	Track etched membranes are formed by irradiating a polymer surface with ions, leading to a consistent pore geometry. Image provided by Mehdi Dehghani (Rochester Institute of Technology). . .	48
2.25	COMSOL modeling of particle capture in a TFF configuration (post run) shows particle deposition on a membrane surface with no set ultrafiltration (Panel A). A comparison with 85% ultrafiltration is shown in Panel B, where more particles deposit on the membrane. Simulation data from Kilean Lucas (University of Rochester). . . .	50
3.1	Microplastic contamination in drinking water from a water fountain. The membrane in the background consists of 8 μ m slits and features a variety of microplastics ranging from fibers to particulates.	55

-
- 3.2 A series of histograms detailing which spot on all slits is occupied when each slit has a specific number of occupants. 58
- 3.3 A diagram detailing an example of how a slit can be sequentially occupied in the model where $t_m = \{3, 5, 2, 4, 1\}$ (for an arbitrary m). Each time a particle lands the dimensions of the channel change, thus changing the resistivity of the slot. In order to avoid computational issues pertaining to $\frac{1}{0}$ errors, the particles used in this model were purposely made slightly smaller than the slit width. 59
- 3.4 Initial pressure rises are marginal as particles accrue on the simulated membrane. This continues until about 80% capacity is reached (roughly 1000s), where we see an inflection point where pressure rises dramatically. 66
- 3.5 Frames over time taken from a recording of a ~ 2800 beads in 50ml PBS experiment. Pressure is stable despite concurrent fouling in the experiment until a critical amount of active membrane area is blocked. The resulting pressure rise is indicative of a membrane capacity, where maintaining flux requires a higher pressure driving force. 68
- 3.6 Frames over time taken from a recording of a ~ 5700 beads in 50ml PBS experiment. The timeframe for inflection occurs earlier than in 2.8k bead experiments. 69
- 3.7 Frames over time taken from a recording of a ~ 28000 beads in 50ml PBS experiment. 70

3.8	As bead concentration increases, pressure inflection points occur earlier in experiments. Increased bead distribution density corresponds to more robust pressure inflections as well as lower uncertainty between experiments.	71
3.9	Across all experiments performed, pressure inflections tend to occur when $\sim 60\%$ of a membrane is occupied.	72
3.10	Frames over time taken from a recording of a $\sim 100,000$ beads in 10ml PBS experiment.	74

1. Introduction

1.1 Silicon Nanomembrane Technology in Microfluidic Devices

Silicon nanomembranes are novel membrane devices that were first discovered in 2007 [1, 2]. Featuring ultrathin, free-standing structures that vary from 10 – 100 nm in thickness, nanomembranes offer robust filtration and separation performance in size and charge based applications compared to thicker conventional membranes. This advantage stems from the fact that nanomembranes are 2-4 orders of magnitude thinner than commercial polymer membranes [3]. This confers lower resistance to transmembrane flow and subsequent lower transmembrane pressures (TMP).

Silicon nanomembranes feature high porosities and a wide range of pore diameters. The manufacturing process used in their creation allows for porosities of 2 - 20% and pore diameters that range from 5 nm – 10 μm . Pore diameter to thickness aspect ratio is 1:1, meaning that the pore diameter and membrane thickness are roughly identical [2]. Not only does this enable improved transport

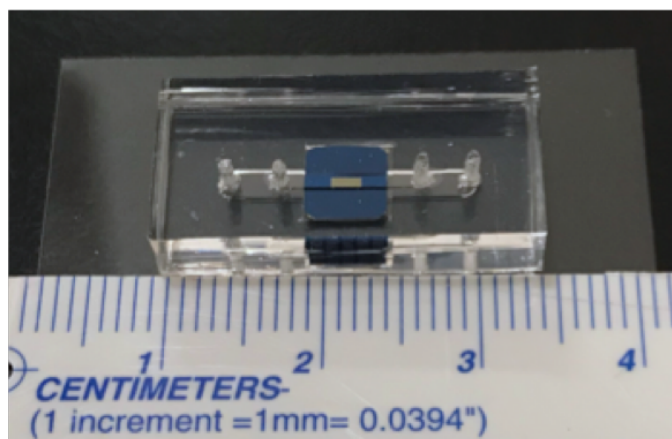


Figure 1.1: A top view of a typical microfluidic device setup featuring an ultrathin silicon nanomembrane chip. The glass slide is 40 mm long and supports the device. The chip featured in this particular device is 2.7% porosity with an average pore diameter of 33.2 nm.

across the ultrathin membrane with lower sample loss and lower transmembrane pressures, it also makes the timescale for diffusion across the membrane negligible. This aspect ratio and the ultrathin nature of silicon nanomembranes also means that the pores in these membranes lack the internal structure and tortuous paths commonly seen in conventional membranes.

Additionally, the ultrathin properties of these membranes allow for both optical and electron transparency, enabling a number of imaging modalities not possible with polymeric membranes. When used in conjunction with microfluidic devices, these membranes provide a highly customizable environment for several different types of experiments. For example, in literature silicon nanomembranes have been used in filtration [4], hemodialysis [5], and biosensing [6]. Silicon membranes are also notable for their biocompatibility, first described in Agrawal et al [7]. This has been used for the creation of systems such as vascular transmigration

models [8].

Two types of silicon nanomembranes were used in this research: ultrathin nanoporous silicon nitride (NPN) nanomembranes and ultrathin microporous silicon nitride nanomembranes. The NPN nanomembranes feature nanoscale sized pores and the microporous membranes have micron scale pores. Both of these types of membranes are manufactured differently. Briefly, NPN is made by depositing silicon nitride masks on both sides of a silicon wafer. On the topside of the wafer, a-Si (amorphous silicon) and silicon dioxide are deposited sequentially. A rapid thermal process (RTP) leads to pnc-Si formation with pores above the silicon nitride layer. After this, the SiO₂ layer on top is removed and the bottom of the wafer is patterned with photolithography to expose the silicon wafer. The top side of the wafer then undergoes reactive ion etching (REI) to transfer the nanopores from the pnc-Si into the silicon nitride layer. REI also removes the pnc-Si layer. The bottom of the wafer is then bulk etched to remove the silicon (note the top layer is protected by an added layer of SiO₂ which is removed after bulk etching) and this leaves a freestanding membrane structure [2]. Microporous ultrathin membranes are made through a photolithography process, so they only use the silicon wafer and nitride masks.

Given the multifaceted capabilities of silicon nanomembranes, understanding their performance is imperative for further research. Thus, this work focuses on understanding how membrane fouling mechanics can be mitigated for performance advantages, specifically with the filtration of protein solutions. Figure 1.1 depicts a typical ultrathin nanomembrane device format for this work. These devices will be

used to assess performance for the purposes of understanding membrane mechanics in tangential flow filtration, mitigation of fouling, and for particle capture.

1.2 Extracellular Vesicles and Cancer Biomarkers

Small, lipid membrane bound particles known as extracellular vesicles (EV) are secreted by cells into their respective environments, ultimately functioning as a means of inter-cellular communication and selective waste elimination [9]. EVs are notable for containing a variety of cellular products that are indicative of their parent cell's metabolic state, including proteins, DNA, and RNA [10] (Figure 1.2). All EVs vary in diameter, however specific diameter ranges exist depending on the location an EV originates from. EVs that are 50 nm - 150 nm in diameter are typically endosomal secretions while EVs up to 1 μm in diameter are formed from the plasma membrane [9]. The smaller EVs originating from the endosome are called "exosomes" while the larger EVs from the plasma membrane are called "microvesicles" [9]. Of these two, exosomes are seen as exploitable for diagnostic medicine since they're commonly found in biofluids such as saliva, blood, or urine [11, 12, 13]. Exosomes contain copious amounts of microRNA (miRNA) content related to their cell of origin [10]. In literature, analysis of miRNA in cancer derived exosomes has shown overexpression of specific miRNA strands versus healthy controls [10].

Given the correlation between miRNA expression and cancer pathogenesis

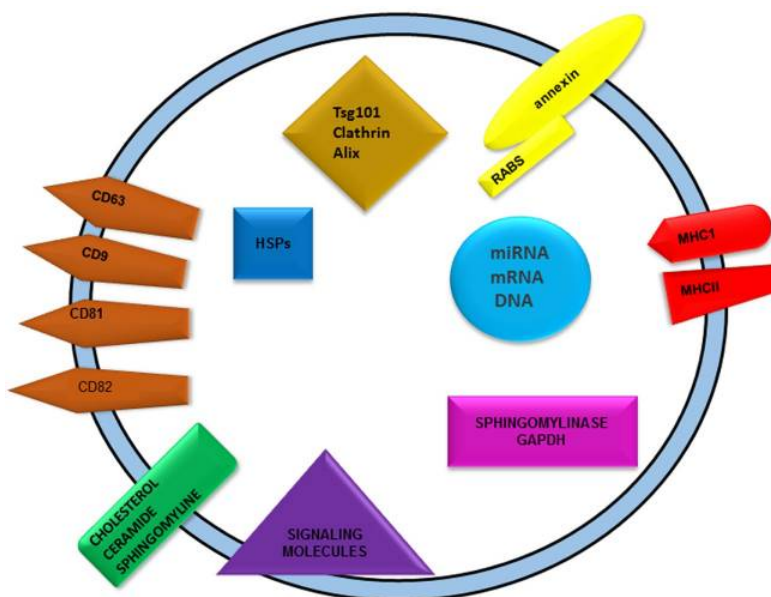


Figure 1.2: A diagram depicting common contents of exosomes adapted from Rajagopal and Harikumar (2018). Nucleic acid assessment, particularly of miRNAs, is a commonly discussed approach to exosome analysis for early cancer detection [10].

[14], capturing and purifying exosomes is useful for their diagnostic potential as early cancer biomarkers. To this end, previous work in this lab has established the concept of "tangential flow for analyte capture" (TFAC) as a means of separating analytes from a biofluid background using tangential flow filtration and silicon nanomembranes [3]. This process is capable of capturing exosomes on a membrane surface through size based separation. More specifically, nanoporous membranes such as track etched polymer membranes and NPN enable this due to having a pore size in the same diameter regime as exosomes. Knowledge gained from this research will assist in refining flow regimes used for TFAC and to optimize exosome capture.

1.3 Tangential Flow Filtration, Critical Flux, and Fouling

Tangential flow filtration (TFF) is a common flow technique used in bioprocessing with membranes [15] where a fluid flows tangentially across the surface of a membrane with some movement of fluid through the membrane itself. Fluid that passes through a membrane is referred to as "permeate" while the non passing remainder is called "retentate" and can be circulated back into a system as needed [16]. Another commonly used technique is dead end filtration where fluid flows normally against a membrane and an attempt is made to pass 100% of the feed fluid. Depending on the characteristics of the membrane used, fluid movement through a membrane can be classified as microfiltration or ultrafiltration. Microfiltration is typically used in sterile filtration with pore sizes as low as $0.1 \mu\text{m}$ and ultrafiltration is commonly used in downstream concentration processing with pore sizes $< 0.1 \mu\text{m}$ [16, 17]. Pore size is not a common delimiter for ultrafiltration membranes, however, as molecular weight cutoff (MWCO) is used to better classify them [18]. Specifically, MWCO is a molecular weight at which 90% of a macromolecule solute is unable to pass through a specific ultrafiltration membrane [18].

Keeping this in mind, this research focuses on using NPN in TFF with syringe pumps facilitating the ultrafiltration of bovine serum albumin (BSA) in phosphate buffered saline (PBS). Dead end filtration with protein rich solutions results in NPN membranes rapidly fouling due to their high permeability and lack of internal structure. Figure 1.3 depicts an example of the robust differences in performance

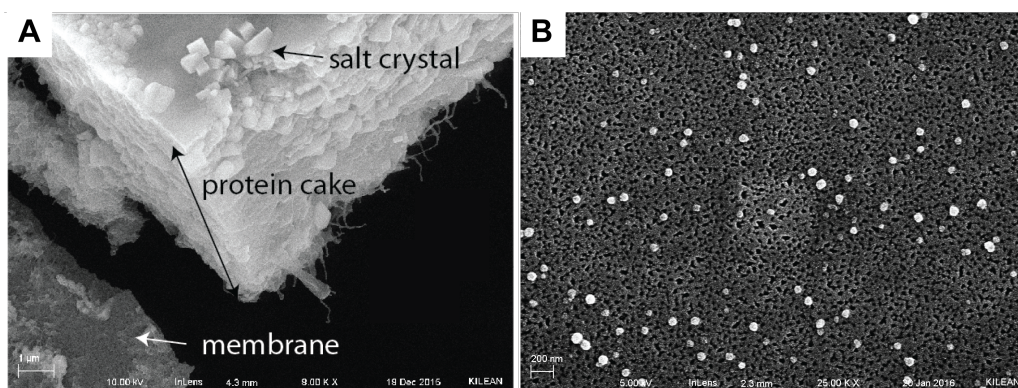


Figure 1.3: Dead end filtration (1.3A) can result in the buildup of protein cakes as thick as $8 \mu\text{m}$ while tangential flow filtration (1.3B) can result in no protein deposition at all. In 1.3A a protein solution at 60 mg/ml was normally flown onto a membrane surface, depositing large amounts of protein in a cake. In 1.3B, protein laced with gold nanoparticles was tangentially flown across the surface of the membrane, leaving no trace of protein behind with only particles on the surface. Imaged by Kilean Lucas (University of Rochester)

for NPN in TFF and dead end filtration. Using TFF avoids the buildup of concentration polarization layers on the membrane surface as species in a fluid are rejected from it [19]. Ultimately, this mitigates protein "cake" formation buildup [20] by removing sites of protein deposition on the membrane surface. The performance gain by using TFF also allows for other useful bioprocessing applications such as removal of impurities [21] and buffer exchanges [22]. A mechanistic example of purification can be seen in Figure 1.4, where particles in a protein solution are captured by an ultrafiltrating membrane with protein simply passing through. Attempting to increase transmembrane flux beyond the capabilities of a membrane can result in fouling with TFF, however, requiring the need to find balance between supply flow rate and ultrafiltration rate in NPN membrane systems.

The concept of critical flux was first defined in Field et al. (1995) as the maximum permeate flux for which a membrane experiences a stable transmem-

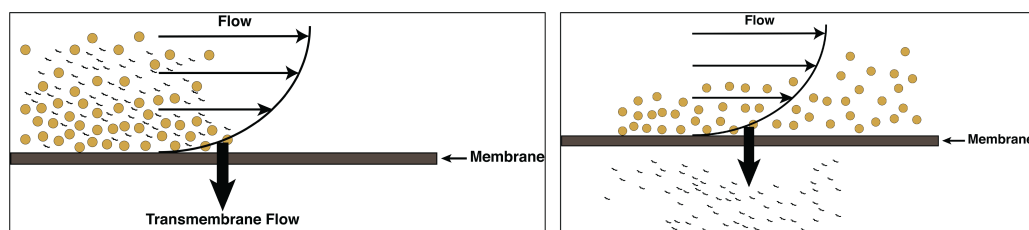


Figure 1.4: TFF with specific flow modes allows for movement of protein through a membrane without cake formation while simultaneously capturing particles in solution. This capture capability is the basis of the "Tangential Flow for Analyte Capture" model currently being developed [3].

brane pressure (TMP) [23] in TFF. Mechanistically, the critical flux is the flux below which a selective membrane undergoing TFF will experience no deleterious fouling or cake formation. An increase in fouling will increase the transmembrane pressure needed to maintain transmembrane flux. Here we posit that pressure dynamics facilitate protein cake formation by driving protein deposition onto a membrane surface. Knowing that conventionally thicker membranes require higher TMPs to facilitate transmembrane flow, our work seeks to systematically assess the hypothesis that ultrathin membranes will exhibit a higher critical flux than conventionally thick membranes due to lower TMPs. The ultrathin nature of silicon nanomembranes is expected to promote "flowing protein cakes" where protein deposition on a membrane surface is minimized compared to thicker membranes. On thicker membranes we expect the formation of "stagnant protein cakes" due to higher TMPs (Figure 1.5). For a robust comparison, NPN will be compared to nanoporous track etched membranes in ultrafiltration.

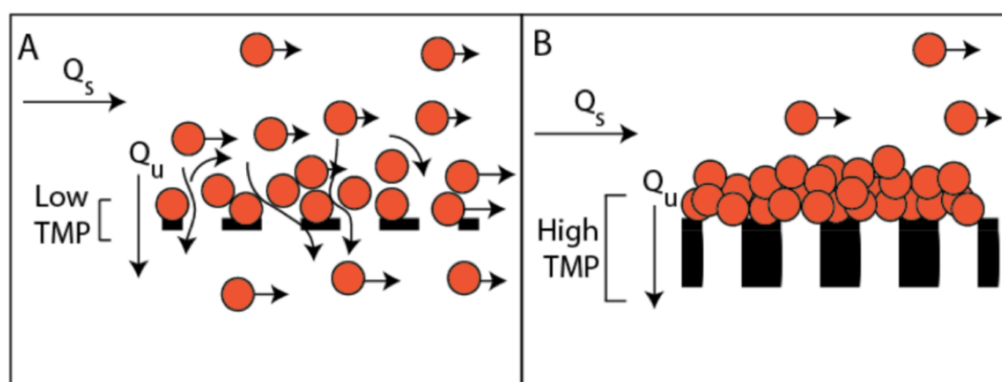


Figure 1.5: In TFF the formation of protein cake layers is facilitated by driving protein towards a membrane surface with higher TMPs enhancing this process. Thicker membranes will experience higher TMPs due to higher resistance to transmembrane flow, thus this research posits that ultrathin membranes will promote the formation of flowing protein cake layers due to lower TMPs and this will increase critical flux.

1.4 Filtering Biologics and Virus Purification

Development of pharmaceutical therapeutics is strictly regulated with high purity requirements, where products that fail to reduce contaminants below specific thresholds face rejection from regulatory bodies [24]. In the development of products such as monoclonal antibodies, viruses face particular scrutiny as microbial contamination is rare with modern techniques [25] and adventitious viral contaminations have been found in common vaccines used for humans [26, 27]. On the other hand, some pharmaceutical applications require concentration of viral vectors for application of advanced medicinal techniques such as gene therapy via adeno-associated virus (AAV) [28]. These situations necessitate robust virus purification techniques in order to reach acceptable clearances. Indeed, in the example of AAV based gene therapy it's been estimated that an acceptable dose

involves 10^{11} to 10^{14} particles [29].

To this end, several techniques exist for virus purification including column chromatography [25], ultracentrifugation [30], precipitation [31], and filtration via membranes [32]. Each of these processes is appropriate depending on the characteristics of the virus being targeted for purification, however filtration with membranes offers robust performance with the potential for higher throughput. Membranes also offer the potential for lowered costs, given that roughly 70% of the cost of production for biopharmaceuticals comes from purification steps [33]. In dead end filtration, commercial membrane technology has been found to be capable of filtering out viruses while retaining > 98% of usable 170 kDa protein product [34]. Membrane technology is not infallible, however, as irreversible fouling from proteins is a concern that limits their continuous usage [34]. Furthermore, if a membrane is being used to purify viruses for a protein based product, validation of clearance is necessary [24]. This makes it impractical to reuse a membrane previously used in a dead-end mode since another independent validation of virus clearance would be required [28].

To mitigate this limitation, tangential flow filtration is an applicable technique since using it inhibits fouling and subsequent buildup of protein cake layers. Under critical flux conditions, a membrane in TFF could run for extended periods of time, providing higher volume output per membrane and lowering costs. Additionally, using TFF with hollow-fiber membranes has shown maintenance of the structural integrity of virus and protein particles [33], making TFF ideal for sensitive virus purification. Ultrathin membranes can enhance processes such as these due to

their thinness and lower resistances to transmembrane flow. Thus, understanding techniques to limit fouling in ultrathin membrane technology adds value to the virus purification process.

1.5 Microplastic Contamination in the Environment and its Physiological Implications

The ubiquitous use of plastics in modern human society has led to significant amounts of pollution, with 60% of all plastics produced (up through 2015) ultimately ending up in landfills [35] and 4.8 to 12.7 million tonnes of plastic ending up in the world's oceans annually [36]. Most plastics are non biodegradable [37], with 92% of all plastics produced (PE, PP, PVC, PET, PUR, and PS) [35] falling into this category. While these plastics do not biodegrade, they do break down in the presence of mechanical weathering [38] and UV radiation [39]. Breaking larger plastic contaminants down does not solve the plastics problem, however, as the end product of these degradative processes are microplastics that spread throughout the environment [40].

Microplastics are small plastic particles that are less than 5 mm long [41] and they are present in common consumer products such as seafood [42], honey, beer, and salt [43]. Studies have shown that humans are commonly exposed to microplastics, with > 90% of particles ingested being excreted as waste [43]. Despite this, many particles remain in the human body and the long term implications of microplastic ingestion on human health are currently unknown due to the recency

of this issue. Concern for human health is growing, however, as microplastic accumulation has been linked to an increase in mortality in aquatic organisms [44]. Furthermore, microplastics have crossed from gut epithelial tissue to the circulatory system of the Mussel species *Mytilus edulis* [45]. Microplastic accumulation also presents avenues for toxin absorption. For example, oceanic microplastics absorb pollutants such as polychlorinated biphenyls (PCB) and hexachlorobenzene [42, 46]. In zebrafish, histological analysis of gills, liver, and the gut indicated localized inflammation caused by microplastic accumulations [47].

These examples necessitate analytical techniques to assess microplastic contamination in frequently ingested products such as drinking water. Note that drinking water is commonly contaminated with microplastics [48, 49]. Thus, ultrathin membranes can enable rapid isolation of microplastic contaminants through TFF or dead end filtration. Analyzing these particles through spectroscopy is accessible as well due to the optically and electron transparent nature of ultrathin membranes and their non plastic construction.

1.6 Thesis Outline and Research objectives

The main focus of this thesis is analyzing the mechanistic contributions of membrane properties, transmembrane pressure, protein concentration, and tangential flow supply rate on critical flux in ultrathin (< 100 nm thick) NPN membranes and subsequently comparing these results to thicker (10 μm thick) TE membranes. Ultrathin membrane capacity with respect to microparticle contamination is also

discussed as well as practical applications of using NPN membrane technology in TFF.

In Chapter 2 we we systematically test the hypothesis that NPN systems outperform track etched membranes by first optimizing NPN based systems in order to promote critical flux. The effect of centrifugation on BSA protein solutions is explored and membrane porosity is evaluated as well. From here a direct comparison is made between NPN and track etched membrane systems as we assess how well their respective systems handle varied protein concentrations and supply flow rate. System transmembrane pressure is evaluated in these experiments as a means to answer a portion of the hypothesis of this research. This chapter ends with a discussion of the concept of membrane capacity, ultimately leading towards the next chapter where a practical application of these membranes is explored.

In Chapter 3 we explore the concept of capacity in microporous membranes by subjecting microfluidic systems featuring microporous membranes to precise experiments with polystyrene beads of various nominal diameters. Specifically, we compare slit membranes to circle pore membranes and seek to define capacity for both while simultaneously exploring mechanistic differences between the two types of pores. We suspect that slit pores will offer a higher capacity since slits are capable of hosting multiple bead occupants while circle pores are only capable of handling one particle at a time. By defining capacity as the threshold bead occupancy when a system experiences a dramatic rise in TMP, we create a readily measurable value for rapid analysis. This chapter ends with a discussion of practical applications of membranes as sensors and analytical tools.

Chapter 4 summarizes the information gained from this thesis and discusses future work and directions to be considered. Namely, testing biofluids and functionalization of ultrathin nanomembrane surfaces are key prospects for future analysis.

2. Critical Flux of Nanoporous Membranes in Tangential Flow Filtration

2.1 Introduction

Ultrathin membranes were first discovered in 2007 [1, 2] and vary from 10 - 100 nm in thickness with highly controllable pore sizes (5 nm - 10 μm). Given that the pore diameter to thickness aspect ratio is 1:1 [2], the membranes lack internal structure often seen in polymeric membranes. This makes ultrathin membranes advantageous for experiments involving filtration [4], hemodialysis [5], and biosensing [6] since they enable improved transport with lower sample loss and TMP. This work will focus on optimizing the critical flux of nanoporous membrane (NPN) systems in TFF of protein solutions, and comparing them with thicker track etched (TE) membranes.

Developing novel strategies of biofluid processing for diagnostic medicine requires an innate understanding of membrane and microfluidic system performance in order to mitigate fouling during filtration processes. To this end, tangential flow filtration (TFF) is frequently used in bioprocessing [15] as a means to avoid

protein cake layer formation [20] during a separation process. Mechanistically, tangentially flowing fluid across a membrane surface with some movement of fluid through a membrane itself avoids build up of concentration polarization layers on the membrane surface [19], thus limiting fouling. TFF is not perfect, however, as certain flow regimes will still promote fouling depending on the properties of the membrane being used. Thus, there is value in optimizing TFF systems such that TMP is stable and no fouling occurs for a given ultrafiltration rate. The maximum flux for which no TMP rise occurs is known as the "critical flux" [23] and allows for continuous membrane usage without deleterious fouling. We posit that lower TMPs in a microfluidic system will enhance critical flux by promoting the formation of "flowing protein cakes" versus "stagnant protein cakes" (Figure 1.5). To assess this, ultrathin silicon membranes will be compared to conventional thicker membrane systems. Since ultrathin membrane systems offer low resistance to transmembrane flow and high porosities, lower transmembrane pressures are needed to drive fluid through the membrane unlike thicker conventional membranes.

2.2 Materials and Methods

2.2.1 Nanoporous Membrane Device Manufacture

Nanoporous Membrane (NPN) microfluidic devices were manufactured in accordance to previous work and literature [50, 51]. Specifically, seven layered components consisting of a 20 x 40 mm glass slide (Corning, Corning NY), four 300 μ m gasket pieces, a NPN chip, and a poly-dimethylsiloxane (PDMS) support

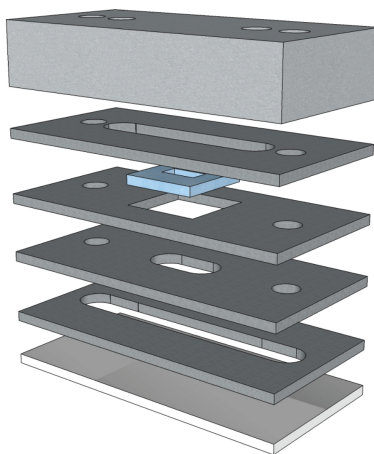


Figure 2.1: A layer diagram of the nanoporous device design featured in this research. A glass slide on the bottom provides rigid support for the gasket layers above it and the PDMS capstone layer provides support for syringe tips. In the middle of the device a membrane can be seen. The gasket layers create two fluid channels that are separated by this membrane.

layer were used to make cohesive microfluidic devices with a membrane barrier (Figure 2.1). The glass layer provides rigid support for the device and acts as a backbone for the bottom channel gasket layer, while the other gasket layers facilitate fluid flow and hold the NPN in place. The PDMS layer provides support for blunt metal syringe tips that are used to connect tubing and syringe pumps to the microfluidic device.

2.2.2 Silicon Gasket Processing

Fabricating microfluidic devices for tangential flow filtration (TFF) required that gasket composite be cut such that stacking multiple layers on one another resulted in the construction of two fluid channels separated by a membrane. Each unprocessed gasket composite piece consists of three components: hard plastic, 300 μm of

usable gasket, and soft plastic. Ultimately the gasket in the middle is used and the two outer plastic portions are discarded. This will be detailed further in the UV Ozone bonding section. To accomplish the goal of creating two fluid channels separated by a membrane, four layers of 300 μm gasket were needed to create (in order from bottom to top) a bottom channel, a chip sealing layer, a chip holding layer, and a top channel. Precise vector diagrams for each layer were drafted in a craft cutter software package (Silhouette, Lindon, UT). The diagrams were designed so that two fluid "inlets" and two fluid "outlets" are made when the layers are stacked on top of each other. This allows for access to both the top channel and the bottom channel of the completed device. Gasket composite was subsequently processed using these blueprints in a CAMEOTM craft cutter (Silhouette, Lindon, UT). After cutting, the gasket composite was cleaned of residue and prepped for UV Ozone bonding. Figure 2.2 details the aforementioned vector diagrams of these layers and demonstrates the flow expected in a device using this setup.

2.2.3 Poly-dimethylsiloxane Preparation

In order to provide support for blunt metal syringe connections at the top of the device, a layer of poly-dimethylsiloxane (PDMS) was needed as 300 μm gasket lacked the rigidity needed to hold syringe tips securely. 25g of PDMS (DOW Consumer Solutions, Midland, MI) was mixed with 2.5g of curing agent (DOW Consumer Solutions, Midland, MI) in a plastic weigh boat. Weights were accurately measured by using a precision lab scale (OHAUS, Parsippany, NJ). This mixture was degassed in a vacuum chamber for one hour to remove most air bubbles present.

Once this process was complete, the mixture was then transferred to a square mold and degassed again in a vacuum chamber for another hour. Afterwards, the PDMS mixture was placed in a 70°C furnace (Barnstead Thermolyne Corporation, Ramsey, MN) and allowed to cure overnight. Once the PDMS was cured, it was cut into 12 by 24 mm blocks. These blocks then had four holes punched into them with blunt syringe tips in order to create the four inlets and outlets featured on these devices.

2.2.4 Nanoporous Membranes

The membrane layer utilized in the device features a chip extracted from a wafer purchased from SiMPore Inc. (Henrietta, NY). Chips extracted from these wafers are 5.4 x 5.4 mm² in size and have an active membrane window slot of 2 x 0.7 mm². The 18.8% NPN used in this research had an average pore size of 65nm and roughly 5 x 10⁷ active pores per membrane. These pore characteristics (as well as others such as porosity) were verified via electron microscopy image analysis conducted in Wolfram Mathematica (Champaign, IL) and Mathworks Matlab (Natick, MA).

2.2.5 UV Ozone Bonding

Each microfluidic device was assembled layer by layer. First, the cutout gasket composite bottom channel layer had its soft plastic removed. The glass slide and the bottom channel layer were then placed in a UV Ozone apparatus (Novascan, Boone, IA) such that the exposed gasket surface was facing upwards and treated for 10 minutes. Afterwards, the glass and gasket were extracted and bonded together,

taking care to avoid air bubbles. The combined layers were then left to cure in the 70°C furnace for one hour. This process was repeated sequentially for each new layer added onto the device, with the hard plastic backing being removed from the combined device on each step. When the membrane needed to be added, a special chip holder was used to ensure that the bottom surface of the chip was UV ozone treated. The last step involved adding the PDMS layer onto the device. Before UV ozone treating PDMS, the blocks were cleaned in a 70% ethanol solution and placed inside a bath sonicator. The blocks were left to sonicate for 2 hours before drying off, being UV Ozone treated, and bonded to the device. The completed devices were left to cure for at least 2 hours in the furnace before use in experiments.

2.2.6 Track Etched Membrane Device Manufacture

Track-Etched membrane microfluidic devices (TE) were manufactured in collaboration with the Gaborski Lab (Rochester Institute of Technology, Henrietta, NY) [3]. The devices were layered in a different manner versus the NPN microfluidic devices, with channels on both sides of the device (Figure 2.3). Briefly, a polycarbonate sheet functioned as the top layer of the device and had a double sided tape layer affixed to it. This tape layer had a channel cut into it and was used to adhere a polymeric TE membrane layer with 80 nm diameter pores. Because of the lower porosity of the TE membranes, the active area of filtration had to be adjusted to achieve a similar number of pores as NPN. Thus, TE membranes had an active area of 4 mm² with $\sim 10^7$ pores available compared to NPN with 1.4 mm² and

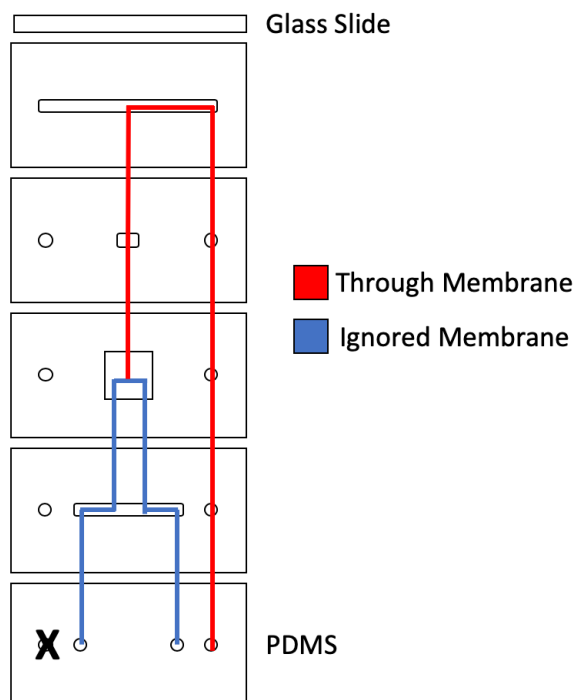


Figure 2.2: Vector image diagram of an NPN microfluidic device with a flow pattern for tangential flow filtration.

$\sim 10^7$ pores available. A gasket layer with another channel was placed on the TE membrane and PDMS was placed on the bottom to provide support. A clamp was utilized in order to fully seal the device.

2.2.7 Protein Serum Preparation

Protein serum was created by weighing 98% purity crystalline bovine serum albumin (BSA) (Sigma Aldrich, St. Louis, MO) in an analytical balance (OHAUS, Parsippany, NJ) and suspending it in 1x Phosphate Buffered Saline (PBS) (Thermo Fisher Scientific, Waltham, MA) in order to yield 50ml of solution. This was done

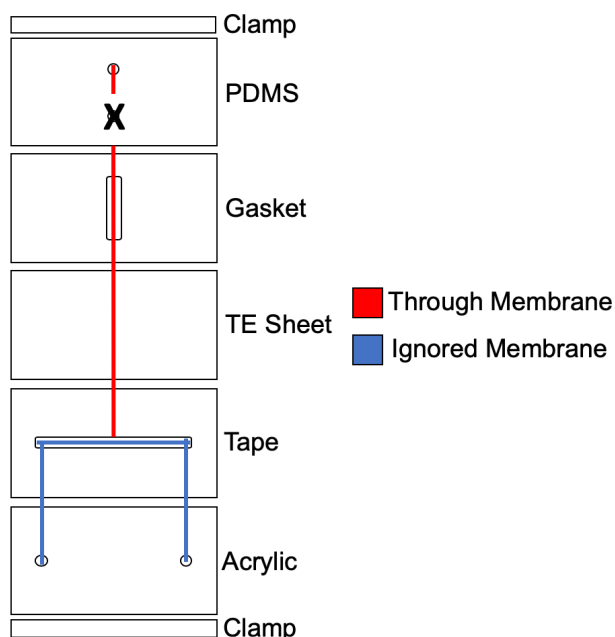


Figure 2.3: Vector image diagram of a TE microfluidic device with a flow pattern for tangential flow filtration. Note in this device there are inlets and outlets on both sides of the device with ultrafiltration occurring through a membrane sheet in a confined area.

for varying concentrations (1mg/ml, 5mg/ml, 10mg/ml, 30mg/ml, and 60mg/ml) depending on the needs of the experimental trial being conducted. Samples were stored at 8°C and left to dissolve for several hours to ensure that the fluid had no visibly undissolved BSA. In order to ensure solution homogeneity, a technique to remove aggregates was needed as unprocessed protein solution rapidly fouled membranes. Originally, a 0.2 micron filter was used to help clean up the BSA solution however this resulted in worse performance. This was likely due to shedding of filter material into the BSA solution. Centrifugation was then used to remove aggregates. Aliquots of 1 ml protein serum were placed in 1.5 ml polypropylene microcentrifuge tubes (Beckman Coulter, Brea, CA). Twelve of

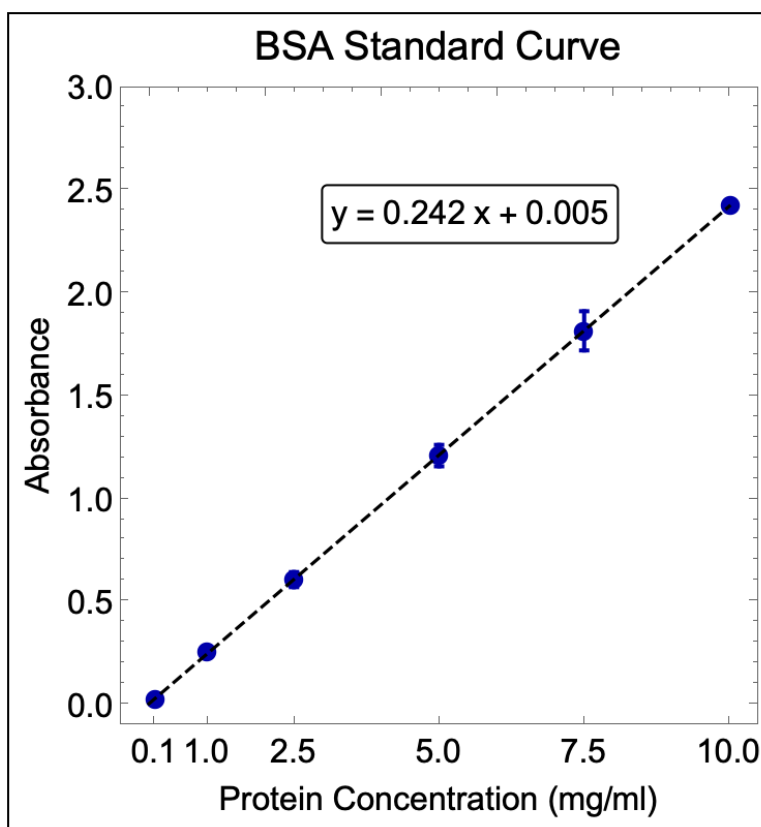


Figure 2.4: A standard curve for BSA suspended in PBS. This was measured by using weighed samples of BSA and used as a point of reference for assessing concentration of processed BSA serum.

these aliquots were spun at a time with an angled (45°) rotor (TLA55, Beckman Coulter, Brea, CA) in an ultracentrifuge (Optima TLX, Beckman Coulter, Brea, CA) at 50,000 RPM for 1 hour at 4°C . The supernatant from these aliquots were extracted via 1ml pipette (Eppendorf, Hamburg, Germany) and stored in a 15ml Falcon conical (Corning Inc., Corning, NY) at 8°C for use in experiments or further processing. BSA concentration post centrifugation was verified with absorption spectroscopy using a Tecan Infinite M200 multimode reader via NanoQuant plate

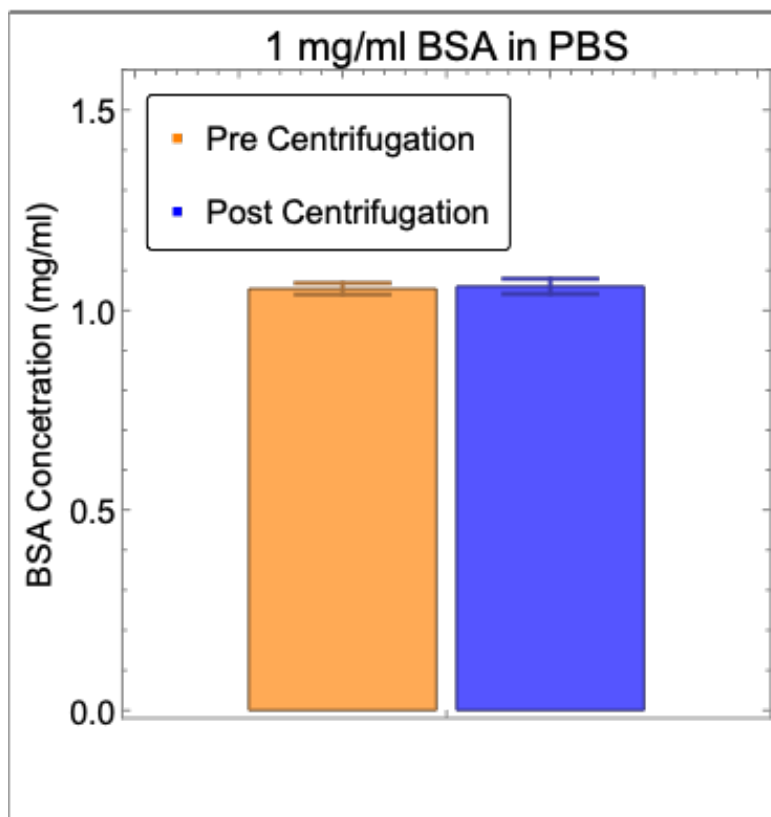


Figure 2.5: 1mg/ml BSA suspended in PBS from multiple samples was aliquoted and measured for protein concentration post centrifugation. The concentration of each sample is still 1 mg/ml, indicating no change in concentration due to centrifugation.

(Tecan, Männedorf, Switzerland). Specifically, a standard curve was made using known weighted concentrations of BSA suspended in PBS (Figure 2.4). This curve was then used to assess the concentration of protein in ultracentrifuged samples. There was no difference in concentration between processed and unprocessed samples (Figure 2.5). Dynamic light scattering of pre and post centrifuged samples was also used, however there was not enough evidence to verify reduction in average particle diameter after centrifugation (Figure 2.6).

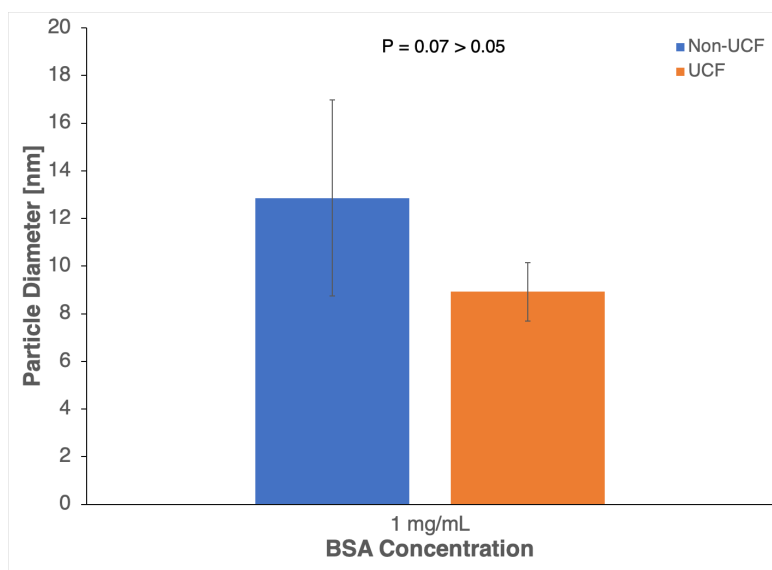


Figure 2.6: DLS analysis of pre and post centrifuged BSA samples lacks enough evidence to suggest a reduction in average particle diameter given that $p > 0.05$ in a paired t-test. The presence of aggregates is later verified through the pressure data in experiments.

2.2.8 NPN Microfluidic Device Overview

The microfluidic devices have a top channel and bottom channel separated by a permeable membrane. Four holes in the PDMS layer allow for access to either end of both of these channels. Fluid enters through the top channel and either passes through the membrane or leaves via the top outlet (Figure 2.7).

2.2.9 Microfluidic System

Microfluidic devices were connected to fluid pumps and a sensor array as depicted in Figure 2.7. Two Fusion 200 syringe pumps from Chemyx (Stafford, TX) were oriented such that one pump was connected the top input side of the device for fluid supply and the other connected to the bottom output side for ultrafiltration. Note

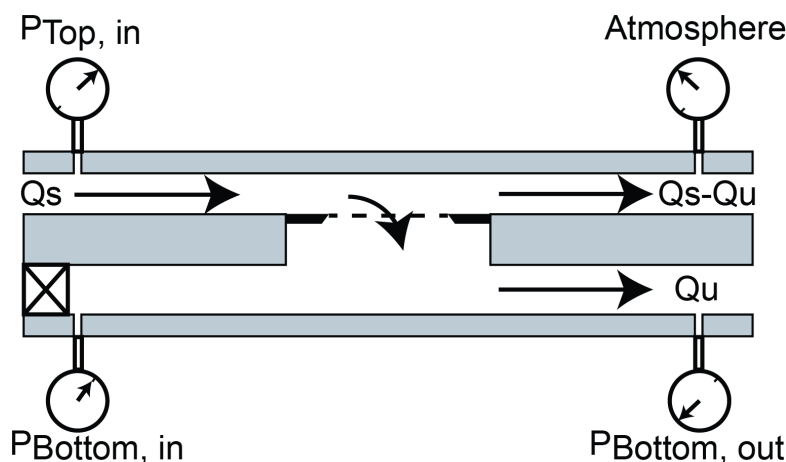


Figure 2.7: A device diagram indicating flow and sensor orientation for all experiments. The bottom inlet (left side) is closed off while the top inlet receives fluid from a syringe pump. Fluid is pulled through the membrane and bottom outlet by another syringe pump.

that a similar orientation was used for TE microfluidic devices, despite differences in location of fluid channel access ports. Plastic syringes of varying volumes (5ml, 10ml, and 60ml) from BD (Franklin Lakes, NJ) were loaded into the supply pump to provide fluid supply depending on the experiments being performed. Experiments that required a higher supply flow rate used syringes with larger volumes while experiments that focused on changes in protein concentration used 5ml syringes. A 5ml syringe was utilized in the ultrafiltration pump for all NPN and TE experiments to ensure consistency with the mechanical force expected by a syringe drawing fluid. All inlets and outlets on the microfluidic device were connected via 4.5cm 1/32" diameter plastic tubing (Cole Parmer, Vernon Hills, IL) to uPS pressure sensors (Labsmith, Livermore, CA) housed in a plastic T-section (Labsmith, Livermore, CA). These sensors were connected to a laptop computer and provided average pressure in both the top and bottom channels. Another 4.5cm

1/32" plastic tubing was utilized on the other end of the t-section for all inlets and outlets. The top inlet was connected to the supply syringe and the bottom outlet was connected to the ultrafiltration syringe. The bottom inlet was clamped off to ensure that any additional fluid in the bottom channel would be pulled through the membrane during the experiment and the top outlet was open to atmosphere as an outlet for waste.

2.2.10 Experimental Process and Data Collection

Data collection utilized a "flux stepping" technique adapted from literature [52], in which ultrafiltration rate (Q_u) increased by 10 percent of the supply rate (Q_s) every 45 minutes for experiments involving NPN and 15 minutes for experiments involving track etched membranes (TE). Note that experiments involving supply flow rate went up by steps of 3 micro litres per minute in order to maintain consistency. The track etched membranes had lower experiment times due to device fragility, in which the devices used were unable to withstand more than 1 to 1.5 hours of constant flow without leaking. This did not effect achieving critical flux, however, as stable transmembrane pressures are rapidly achieved between steps. A GUI was written to control the syringe pumps for single flow experiments while multi-step experiments were done with built in controls on the pumps themselves. The attached pressure sensors collected data at a rate of 2Hz via Labsmith software (uProcess) and this data was then saved into a .CSV file. A script written in Mathematica analyzed and plotted .CSV files from the data collection software and was also used for all graphs created.

2.2.11 Membrane Chip Analysis and Statistics

Transmission Electron Microscopy (TEM) images of the NPN used in this experiment were analyzed in Mathematica in order to extract useful statistics about the pores. A morphological feature extraction algorithm was written and used to extract pores and other blob type objects from their high contrast backgrounds. These images were then manually classified into four categories (noise, pore, divot, cutoff) for the purpose of creating a training set. Positive pore detections were considered "class 1" and "class 3" detections while classes 0 and 2 were discarded from analysis. Class 3 objects (cutoffs) were any pores that were cutoff from the frame of the camera and were utilized in calculating porosity only. Using this labeled set of $n = 808$, a model using a Random Forest classifier was trained with a loss of 0.290 ± 0.027 and an accuracy of $93.4 \pm 2.6\%$. The trained model was then used as a means to parse through feature detections on TEM images of NPN and extract positive pore detections for further analysis. Another script analyzed these positive detections and provided relevant statistics such as average pore diameter (~ 60 nm) and porosity ($\sim 18.8\%$).

2.2.12 Nanoparticle Sample Preparation

Nanoparticles of various nominal diameters (30nm, 60nm, and 100nm) from BBI Solutions (Crumlin, UK) were used for particle capture and critical flux experiments. Dilutions of 10^7 , 10^8 , and 10^9 beads were made and suspended in a 1 mg/ml protein solution (BSA in PBS) to prevent the formation of bead aggregates.

2.2.13 Definition of Critical Flux and Mathematical Methods

A membrane system is in critical flux as long as $\Delta \text{TMP} < 50\%$ in 30 minutes for NPN experiments and $\Delta \text{TMP} < 50\%$ for 10 minutes for TE experiments. A script was written to parse through data for each trial and calculate change in TMP for each flux step. Since the experiments performed had similar time scales between critical flux steps, the script analyzed the same time frames for NPN and TE data respectively, reporting failures in meeting critical flux criteria as needed. All pressure data presented in graphs has been processed with a mean shift filter to reduce noise.

2.3 Results

2.3.1 Optimizing Critical Flux in Nanoporous Systems

Initially we sought to optimize conditions under which critical flux could occur in microfluidic systems featuring nanoporous membranes. Control experiments using PBS shows that stable transmembrane pressure regimes can occur on a low (2.7%) porosity membrane with an average pore size of 33.2nm (Figure 2.8). In these stable TMP regimes a relationship between TMP and ultrafiltration rate is observed, where stable TMP increases as ultrafiltration rate increases. Protein experiments were first performed on low porosity membranes with unprocessed 1 mg/ml BSA suspended in PBS. This fluid was used in tangential flow filtration at

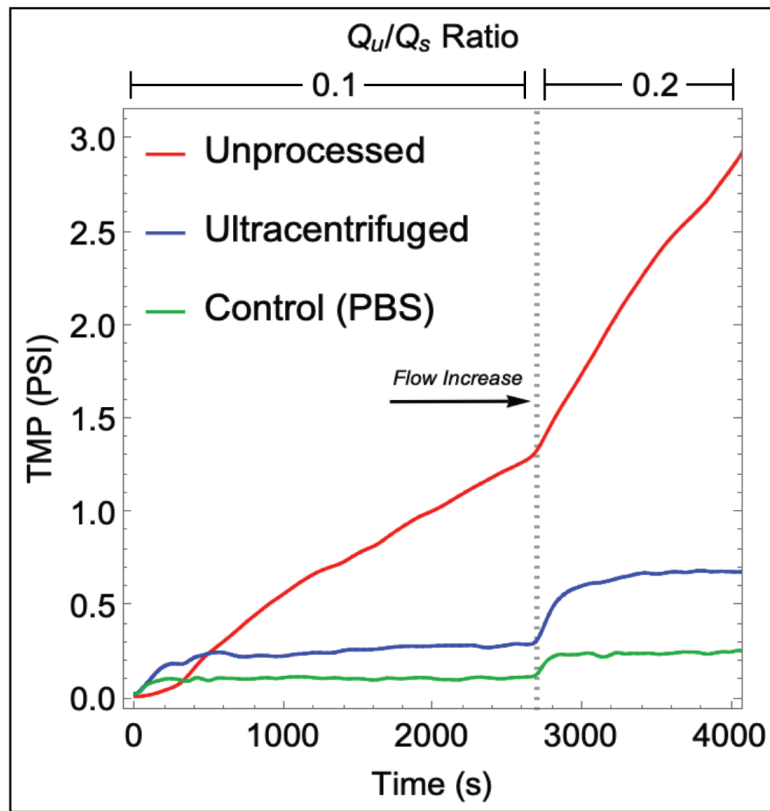


Figure 2.8: Pressure data detailing the effect of centrifugation of BSA samples on critical flux. Experiments performed on a 2.7% porosity membrane show stable transmembrane pressure regimes post centrifugation that are comparable to control experiments.

$Q_s=30\mu l/min$ and $Q_u=10\% Q_s$ every 45 minutes. As seen in Figure 2.8, results were unfavorable as immediate rapid increases in transmembrane pressure occurred at an ultrafiltration ratio $\frac{Q_u}{Q_s} = 0.1$. Centrifugation to remove aggregates (Figure 2.5) provided results closer to control experiments with stable TMP regimes.

Knowing that removal of aggregates is key for inducing critical flux in NPN microfluidic systems, the next property assessed was membrane porosity. Additional experiments were conducted with NPN at 6.6% porosity and 18.8%

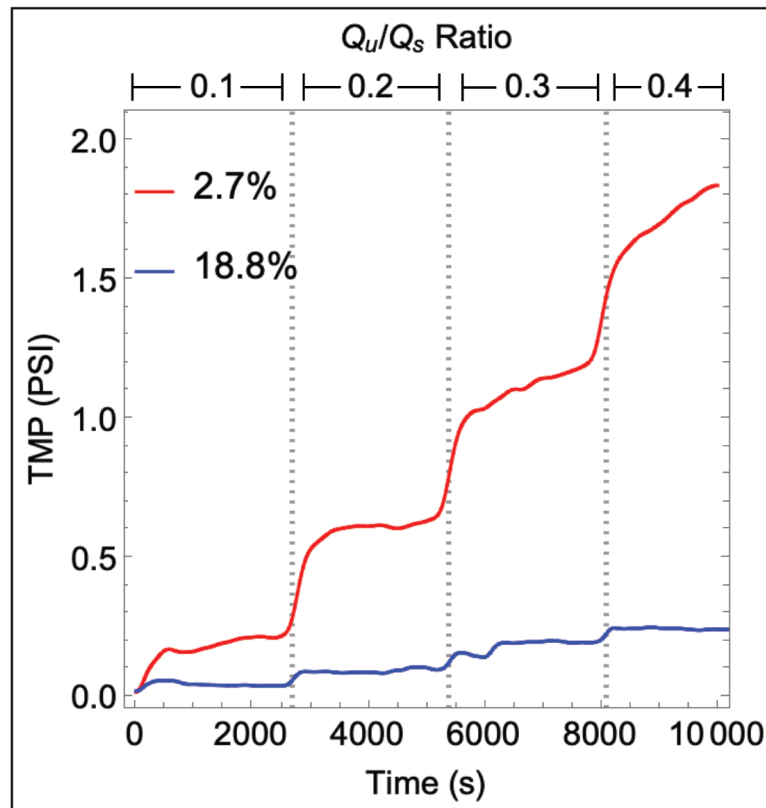


Figure 2.9: Pressure data detailing the effect of porosity on critical flux. Experiments were performed on a 2.7% porosity membrane and an 18.8% porosity membrane. Higher porosity allows the system to achieve better performance in the form of a lower TMP.

porosity featuring pores with an average diameter of 50nm and 65nm respectively and compared to the 2.7% membrane. As porosity increases, critical flux ratio increases as well. The 2.7% porosity membranes had critical flux ratio $\frac{Q_u^*}{Q_s} = 0.283 \pm 0.048$, the 6.6% porosity membrane had $\frac{Q_u^*}{Q_s} = 0.367 \pm 0.067$, and 18.8% membranes featured the highest critical flux ratio at $\frac{Q_u^*}{Q_s} = 0.967 \pm 0.033$ (Figure 2.10). When directly comparing the highest and lowest porosity membranes, critical flux at any level had lower TMPs (Figure 2.9). The intermediate porosity

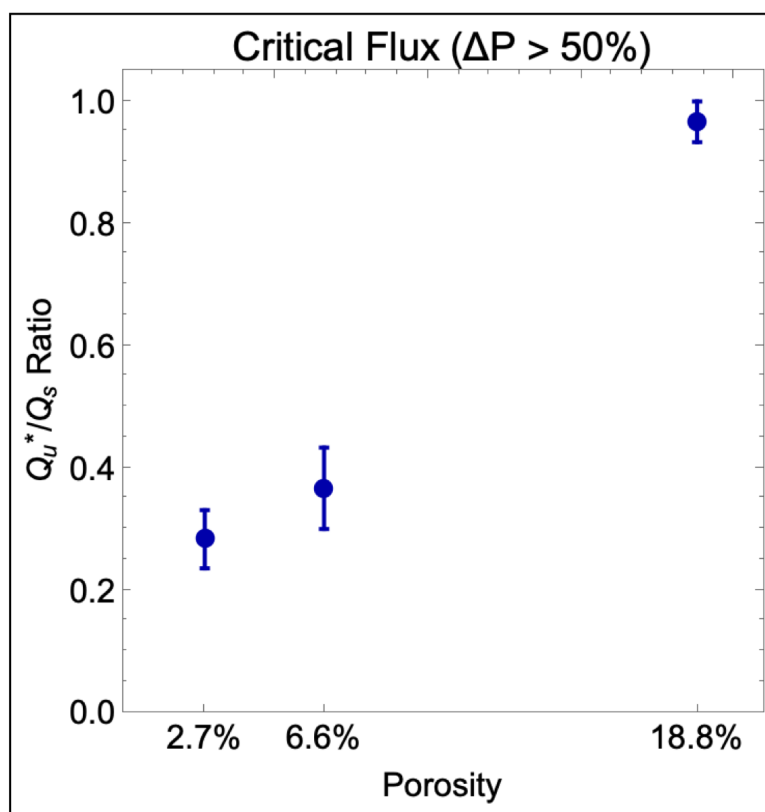


Figure 2.10: Critical flux results for NPN of varying porosities. Higher porosity membranes elucidated higher performance with respect to centrifuged 1mg/ml BSA suspended in PBS.

had intermediate performance, as expected. With these results in mind higher porosity membranes were selected for use in all further experiments.

2.3.2 Effect of Varying Protein Concentration and Supply Flow Rate

After optimizing conditions for the study of critical flux with ultrathin membranes, parameter sweeps with respect to the concentration of protein solution being used

and the top channel flow rate were performed. Higher protein concentrations were used to assess the feasibility of analyzing undiluted biofluids. More specifically, protein concentrations used in this research were designed as dilutions of human blood plasma (60 mg/ml), so 60, 30, 10, 5, and 1 mg/ml were assessed. Faster supply rates were used to assess if faster flowing protein serum would inhibit protein cake formation on membrane surfaces. The supply rates chosen for this assessment were 15, 30, 60, 90, and 120 $\mu\text{m}/\text{min}$.

Results from increasing protein concentration initially showed no changes in critical flux capability (Figure 2.11). The NPN based microfluidic systems were capable of near dead end filtration ($\frac{Q_u^*}{Q_s} \sim 1.00$) with no discernible rise in TMP up to 10 mg/ml protein concentration. Beyond that, we begin to see reduced critical flux performance at 30mg/ml and 60mg/ml with $\frac{Q_u^*}{Q_s} = 0.367 \pm 0.033$ and $\frac{Q_u^*}{Q_s} = 0.200 \pm 0.058$ respectively.

Given that 30mg/ml BSA was the first concentration level to require a tangential component to maintain critical flux with NPN, the potential benefit of increasing supply flow rate was assessed at this concentration. Results are shown in Figure 2.12, noting that Q_u^* is critical flux rate and $\frac{Q_u^*}{Q_s}$ is critical flux ratio. Initial increases in supply rate from 15 $\mu\text{l}/\text{min}$ to 30 $\mu\text{l}/\text{min}$ displayed a critical flux ultrafiltration rate increase of 120%. This percentage increase maintains a consistent critical flux ratio, however, with $\frac{Q_u^*}{Q_s} = 0.333 \pm 0.067$ for 15 $\mu\text{l}/\text{min}$ and $\frac{Q_u^*}{Q_s} = 0.367 \pm 0.067$ for 30 $\mu\text{l}/\text{min}$. Increasing supply rate beyond this showed little benefit as going from 30 to 60 $\mu\text{l}/\text{min}$ resulted in a 27% increase in critical flux rate but a decrease in critical flux ratio $\frac{Q_u^*}{Q_s}$ from 0.367 ± 0.067 to 0.233 ± 0.017 .

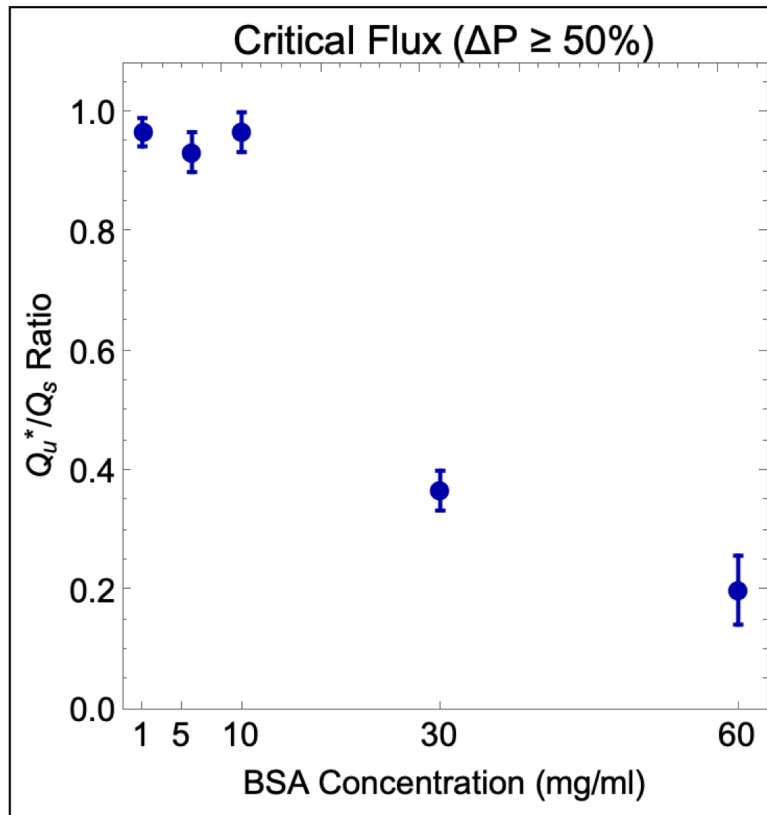


Figure 2.11: Critical flux results for varying BSA concentrations between 1mg/ml and 60mg/ml incident upon an 18.8% porosity membrane. Dead end filtration was possible up to BSA concentrations of 10mg/ml, while at 30mg/ml and 60mg/ml critical flux ratios dropped off accordingly.

Further increases in supply rate result in no performance gain, with critical flux ultrafiltration rate plateauing around 13 -14 $\mu\text{l}/\text{min}$ and critical flux ratio decreasing as supply rate increases.

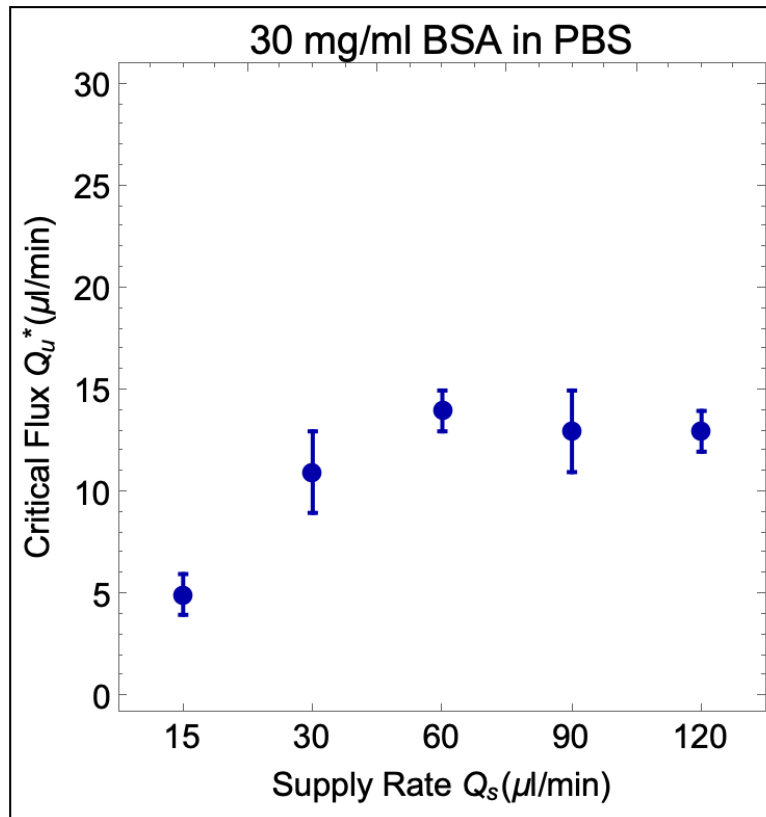


Figure 2.12: Critical flux results for varying supply rate Q_s for the purpose of preventing protein cake formations on the top surface of the membrane. Note that critical flux in this case isn't represented by a ratio rather a specific value. Small increases in supply rate provided slightly improved critical flux rates however there are diminishing returns at higher supply rates. Overall critical flux ratio decreases, however, signifying the advantage of using a slower supply rate.

2.3.3 Comparing NPN performance to Track-Etched Membranes

With NPN critical flux performance established, data was then gathered from TE membranes for comparison. Experiments were performed for both varied protein concentrations and increased supply rate. For protein concentration, supply rate was the same as NPN experiments with $Q_s = 30\mu\text{l}/\text{min}$ and Q_u increasing by $10\%Q_s$

every 15 minutes. Across all experiments performed, TE devices had lower critical flux ratios ($\frac{Q_u^*}{Q_s} = 0.433 \pm 0.067$ at 1 mg/ml BSA, $\frac{Q_u^*}{Q_s} = 0.167 \pm 0.067$ at 5 mg/ml BSA, and $\frac{Q_u^*}{Q_s} = 0.067 \pm 0.033$ at 10 mg/ml BSA) with no critical flux occurring at protein concentrations of 30 mg/ml and 60 mg/ml (Figure 2.13). Given 1 mg/ml BSA was the lowest concentration that needed a tangential flow component to achieve critical flux in TE systems, and since the critical flux ratio $\frac{Q_u^*}{Q_s}$ in TE systems at 1 mg/ml is comparable to NPN systems at 30 mg/ml (0.433 ± 0.067 vs 0.367 ± 0.033 respectively), 1 mg/ml BSA concentration was selected for varied supply rate experiments in TE systems.

In contrast to NPN membrane systems, a faster supply rate actually reduced both the critical flux rate and ratio with TE membranes (Figure 2.14). Initially, flowing slowly at 15 $\mu\text{l}/\text{min}$ with TE membranes resulted in a high critical flux ratio with $\frac{Q_u^*}{Q_s} = 0.867 \pm 0.067$. As supply rate increased, however, observed critical flux rate and ratio were lower. Going from $Q_s = 15$ to 30 $\mu\text{l}/\text{min}$ reduces critical flux ratio to $\frac{Q_u^*}{Q_s} = 0.400 \pm 0.058$ and critical flux rate from 13.0 ± 1.0 to 12.0 ± 1.7 $\mu\text{l}/\text{min}$. Further critical flux decreases occur at $Q_s = 60$ $\mu\text{l}/\text{min}$ ($Q_u^* = 7 \pm 4$ $\mu\text{l}/\text{min}$, $\frac{Q_u^*}{Q_s} = 0.117 \pm 0.067$), $Q_s = 90$ $\mu\text{l}/\text{min}$ ($Q_u^* = 5 \pm 1$ $\mu\text{l}/\text{min}$, $\frac{Q_u^*}{Q_s} = 0.056 \pm 0.011$), $Q_s = 120$ $\mu\text{l}/\text{min}$ ($Q_u^* = 4 \pm 1$ $\mu\text{l}/\text{min}$, $\frac{Q_u^*}{Q_s} = 0.033 \pm 0.008$).

Differences in NPN and TE performance can be elucidated from observing pressure data from TE experiments and comparing them directly to NPN pressure data. Figure 2.15 depicts a comparison between NPN and track etched membranes at a critical flux of 15 $\mu\text{l}/\text{min}$ with 1 mg/ml BSA. NPN displays a 5.67x performance advantage over track etched membrane systems with an average TMP of

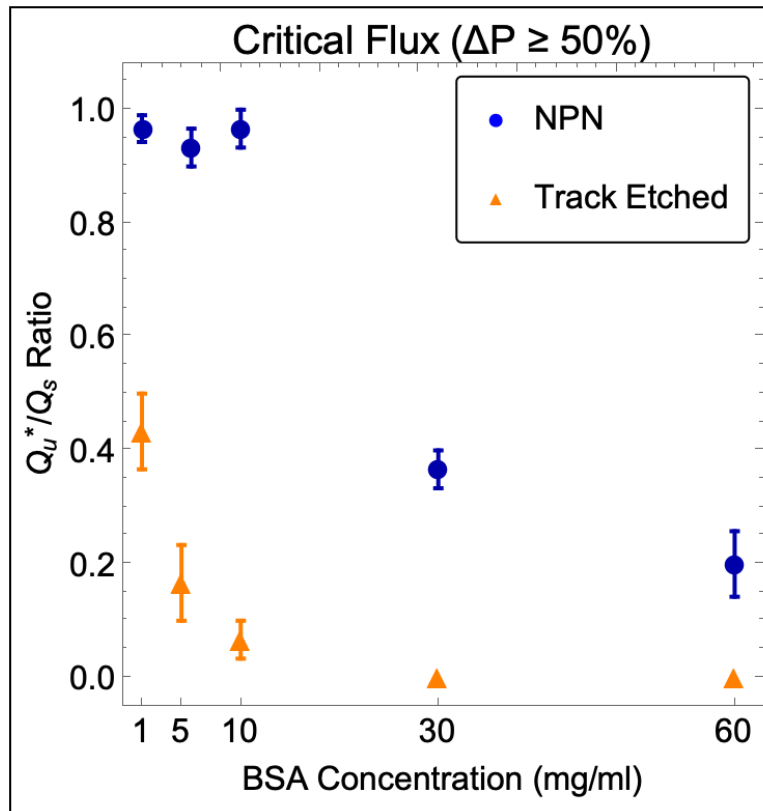


Figure 2.13: Critical flux results for varying BSA concentration with both track etched membranes and NPN results. Track etched membranes have significantly lowered performance across the board. Note that 30mg/ml BSA on NPN and 1mg/ml BSA on Track Etched membranes offer similar performance with respect to critical flux ratio.

0.193 \pm 0.006 PSI versus 1.125 \pm 0.193 PSI. This advantage is maintained even at significantly higher protein concentrations. Figure 2.16 depicts pressure data for experiments at $Q_s = 15 \mu\text{l}/\text{min}$ and $Q_u^* = 3$ and $6 \mu\text{l}/\text{min}$ for NPN at 30 mg/ml and TE at 1 mg/ml. Despite a 30x increase in protein concentration, TMP in NPN membranes are lower than TE devices. Specifically, at $Q_u^* = 3 \mu\text{l}/\text{min}$ TMP in NPN was 0.233 \pm 0.046 PSI versus 0.918 \pm 0.019 PSI in TE. At $Q_u^* = 6 \mu\text{l}/\text{min}$ TMP in NPN was 0.261 \pm 0.018 PSI versus 1.691 \pm 0.051 PSI in TE. Part of the

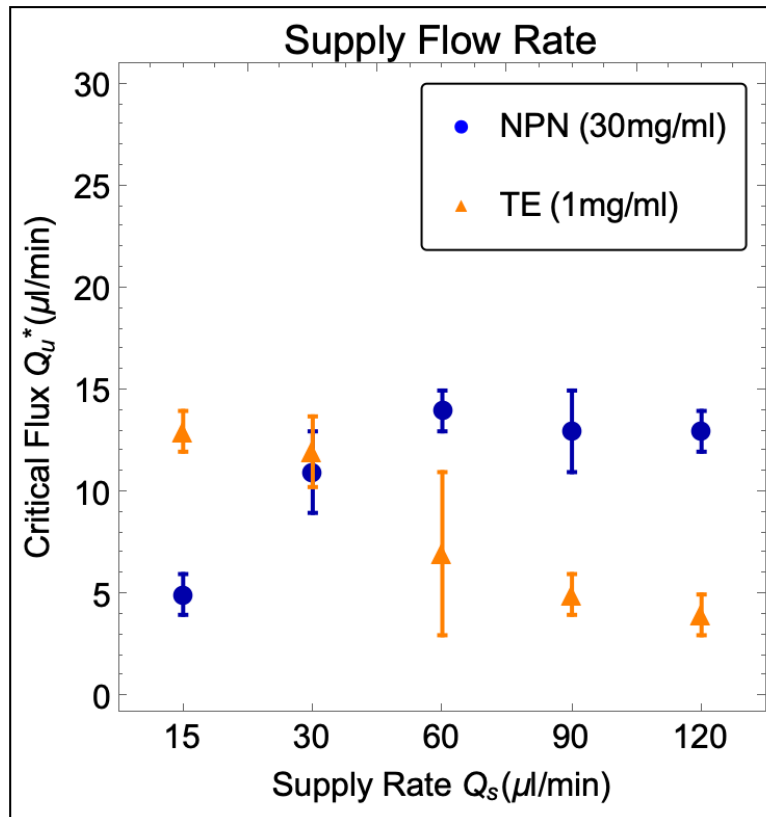


Figure 2.14: Critical flux results for varying supply rate Q_s on both NPN and track etched membranes.

driving mechanism for poor membrane performance in track etched membranes comes from a high initial transmembrane pressure. We define this by looking at the average TMP in the first ten seconds of an experiment and comparing results. In Figure 2.17 we see the effect of increasing supply rate on TMP in both TE and NPN systems. for TE membranes, initial transmembrane pressure increases dramatically as supply rate increases, likely deforming the polymeric structure of these membranes and causing the subsequent decrease in critical flux performance seen in Figure 2.14.

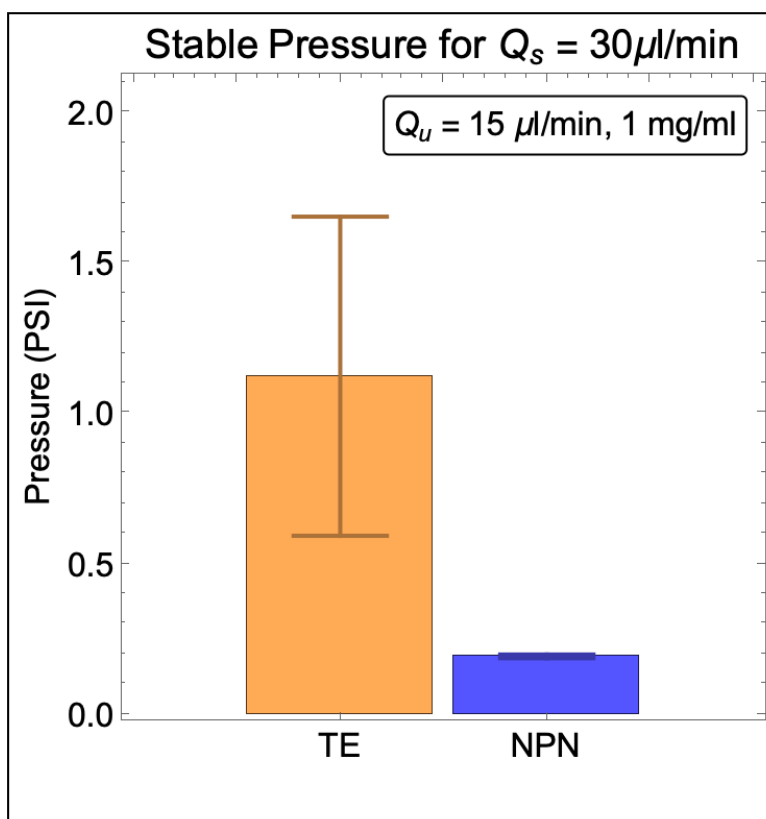


Figure 2.15: Stable pressure data for a critical flux of $15 \mu\text{l}/\text{min}$. NPN based systems exhibit robust performance with lower transmembrane pressures than track etched systems at similar protein concentrations.

2.3.4 Critical Flux Experiments with Gold Particle Capture

To model the presence of particulate in complex biofluids, $1 \text{ mg}/\text{ml}$ BSA with gold nanoparticles were used in TFF experiments featuring NPN membranes. Initial experiments sought to capture particles in pores and see how critical flux was effected. We originally ran experiments with 60 nm particles, matching the average pore diameter of the NPN used in this research. Experiments that matched

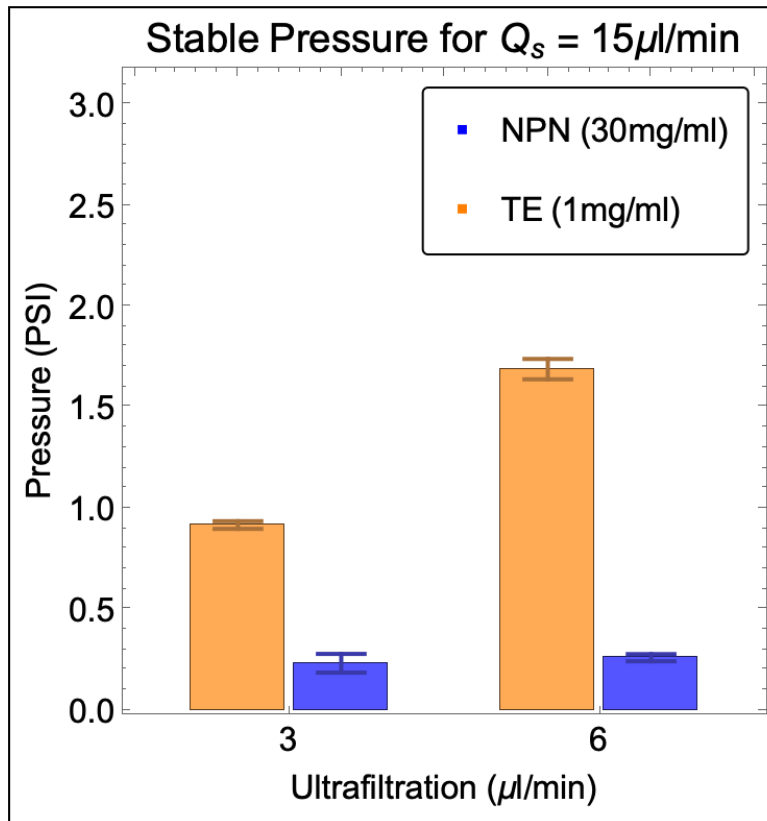


Figure 2.16: Stable pressure data for two critical flux values ($3 \mu\text{l}/\text{min}$ and $6 \mu\text{l}/\text{min}$). Even with thirty times more BSA in solution, NPN based systems exhibit still outperform their track etched counterparts with a lower transmembrane pressure.

particle concentration with the number of open pores on the membrane (10^7 particles for 10^7 pores) showed that achieving critical flux was still possible with $\frac{Q_u^*}{Q_s} = 0.525 \pm 0.048$ (Figure 2.18). Increasing particle concentration by orders of magnitude maintains critical flux capability, despite hypothetically saturating the membrane. At 10^8 60 nm particles $\frac{Q_u^*}{Q_s} = 0.233 \pm 0.033$ and at 10^9 60 nm particles $\frac{Q_u^*}{Q_s} = 0.133 \pm 0.033$, indicating that particles were still passing through the membrane. This was further verified by assessing the color of the permeate, which

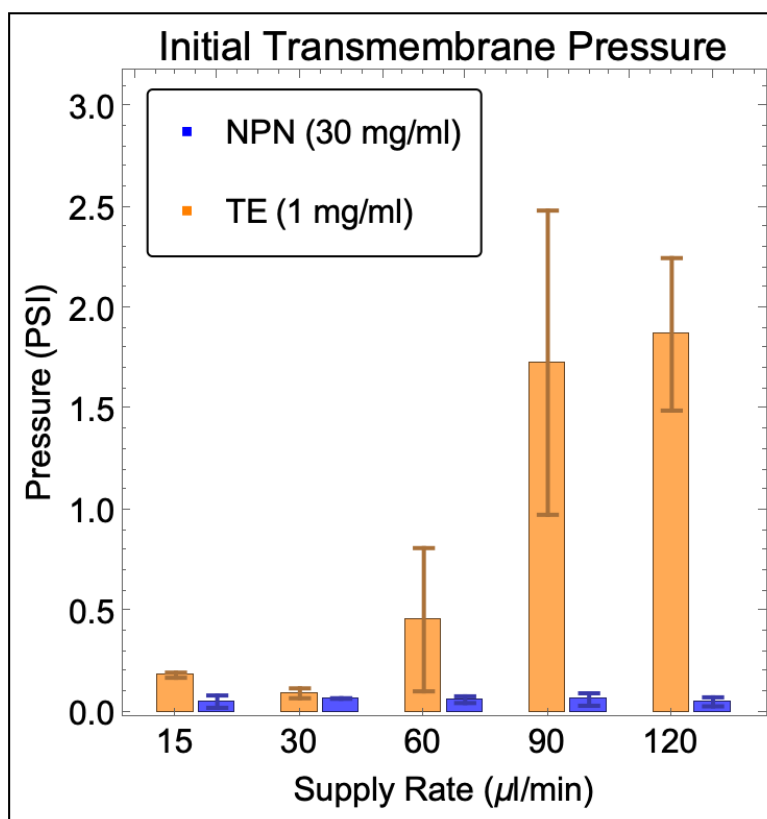


Figure 2.17: Initial transmembrane pressure values for the varied supply rate experiments featuring NPN and track etched membranes. The NPN data comes from experiments conducted with 30mg/ml BSA in PBS and the track etched data includes 1mg/ml BSA in PBS. Increasing supply rates resulted in negligible TMP changes in NPN while track etched systems experienced rapid increases in TMP.

was the same color as the gold particle laced BSA. With mixed particle (60nm and 100nm) experiments, critical flux was slightly reduced versus 60nm particles alone at a concentration of 10^7 particles with $\frac{Q_u^*}{Q_s} = 0.333 \pm 0.067$. Increasing the concentration of mixed particles by an order of magnitude resulted in immediate TMP rise without critical flux, indicating successful fouling and capture.

For all 60nm particle experiments at a concentration of 10^7 particles, $\sim 80\%$

of the particles were captured in pores with no protein cake formation. Figure 2.20 depicts a TEM image of a membrane under these experimental conditions. Another set of experiments were performed with 30nm gold particles. Figure 2.19

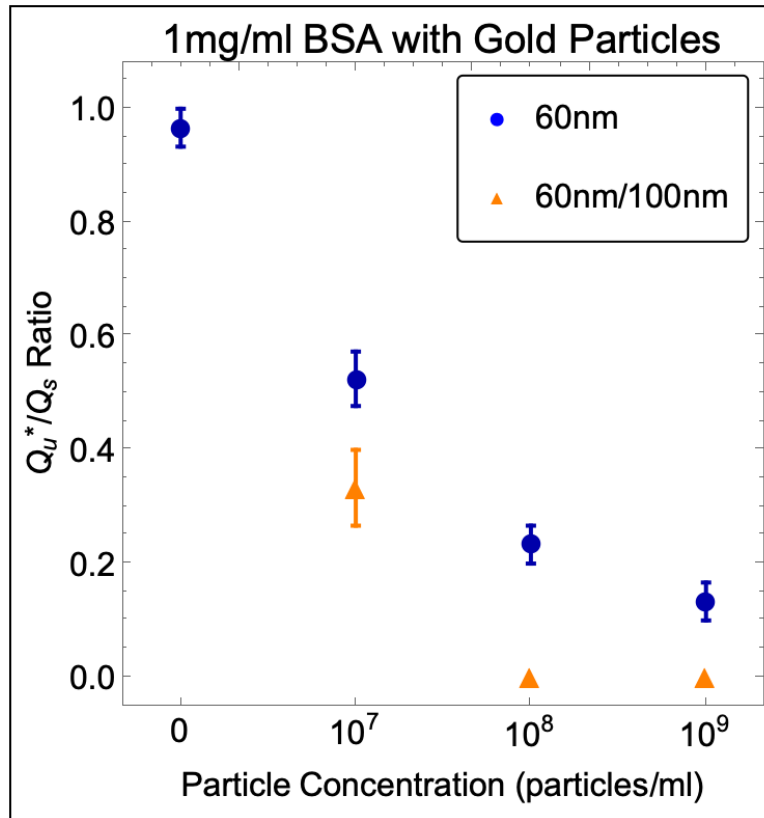


Figure 2.18: Critical flux experimental data for particle laced biofluid experiments. The NPN featured in this research has 10^7 pores available so the first set of experiments matched this number for nanoparticle concentration. Both single and mixed particles were capable of achieving critical flux at this concentration, however increasing concentration by an order of magnitude resulted in an inability to attain critical flux for mixed particle experiments.

shows these experiments. As expected, no changes in critical flux occurs with the addition of smaller particles as they simply pass through the membrane.

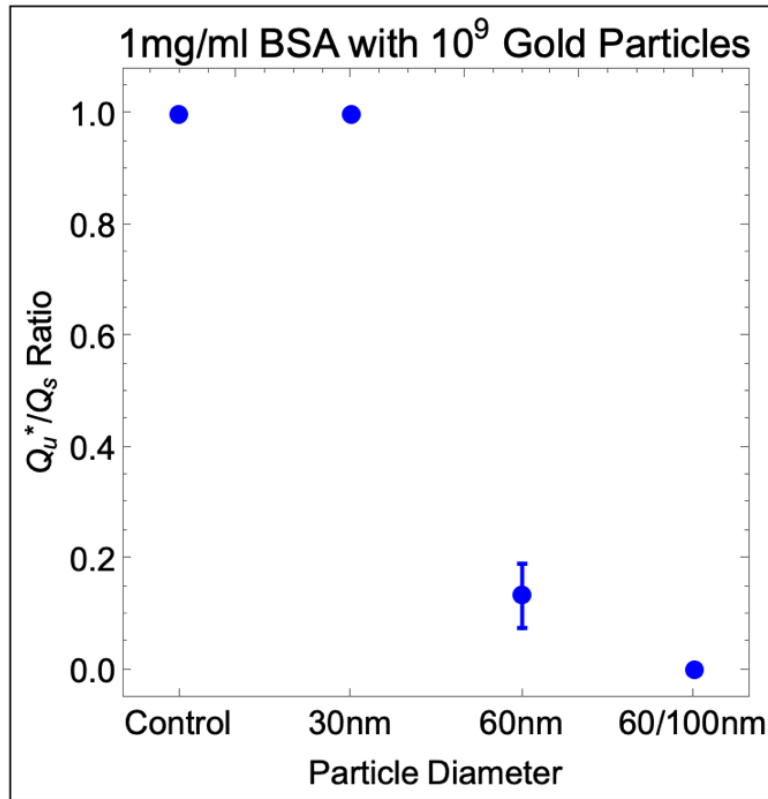


Figure 2.19: Critical flux experimental data for particle laced biofluid experiments at a concentration of 10^9 particles. 30nm particles passed through the membrane without incident while 60nm and 60/100nm mixed particle experiments had poor critical flux performance in comparison.

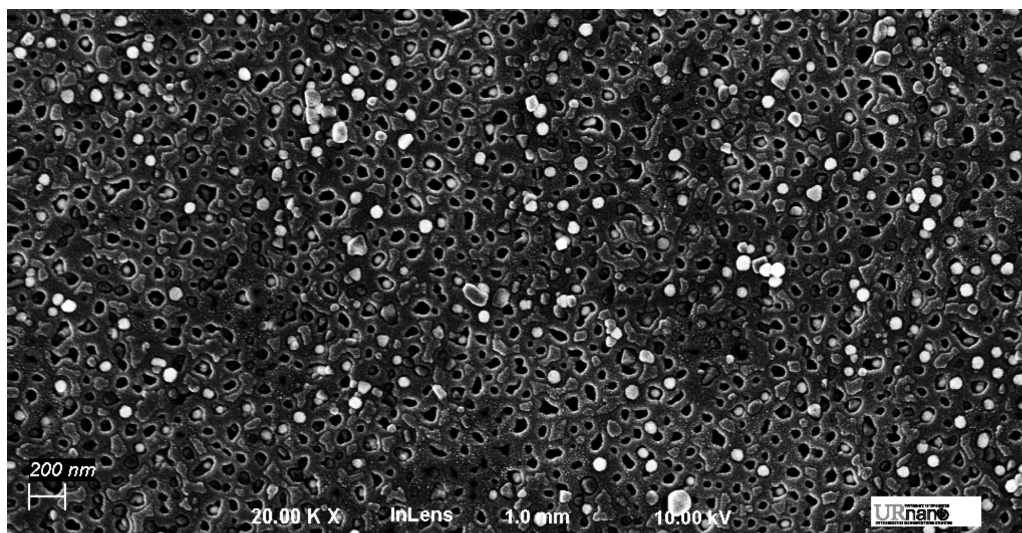


Figure 2.20: TEM imagery of NPN after an experiment with 10^7 gold nanoparticles suspended in 1mg/ml BSA in PBS incident upon its surface. A capture efficiency of 80% is shown here with no visible protein cake formation.

2.4 Discussion

In this chapter we systematically addressed the hypothesis that ultrathin (< 100 nm thick) nanoporous membranes exhibit a higher critical flux in TFF of BSA solutions than conventionally thick (10 μm thick) TE membranes. Increasing membrane porosity to 18.8% and removing BSA aggregates by centrifugation enhanced the critical flux achieved with NPN, providing a base protocol for all future experiments. In TFF, 18.8% porosity NPN membranes were capable of near dead end filtration up to 10 mg/ml BSA and required a tangential component to flow for critical flux at 30 and 60 mg/ml BSA concentration. In contrast, TE membrane systems needed TFF starting at 1 mg/ml BSA and were incapable of achieving critical flux at 30 and 60 mg/ml BSA. Supply rate increases at 30 mg/ml BSA resulted in moderate critical flux rate gain in NPN systems up to $Q_s = 60 \mu\text{l}/\text{min}$ with a plateau afterwards. TE systems with 1 mg/ml BSA experienced a decline in critical flux rate as supply rate increased, which is explained by pressure data where NPN systems had lower TMP than TE systems for all experiments performed. The following sections provide some additional perspective on these studies and their implications.

2.4.1 Protein Pre-filtration, Membrane Porosity, and Critical Flux Performance

Every experiment performed in this research relied on centrifuged BSA since low porosity NPN was generally incapable of maintaining critical flux even at low $\frac{Q_u}{Q_s}$

ratios. This is expected given that deposition of BSA aggregates on the top surface of a membrane are a principle mechanism of membrane fouling [53] with protein microfiltration. Literature has shown that pre-filtration of BSA solutions to remove aggregates has increased flux performance since aggregates and denatured proteins act as building sites for further protein deposition [54]. Knowing this, we sought to use similar techniques in this study to limit fouling. Originally BSA solutions were processed with a $0.2\mu\text{m}$ filter, however this actually led to worse performance with NPN. We suspect that this is likely due to the polymeric filters shedding material into the BSA solution that ultimately makes it way to the surface of the membrane, acting as a catalyst for fouling. Given that NPN membranes lack the interconnected channel structure of the polymeric membranes used in literature and are ultrathin, NPN is highly sensitive to such intrusions. With ultracentrifugation we avoid the issue of material shedding and successfully increased membrane critical flux performance without compromising protein solution concentration.

2.4.2 The Relationship Between Porosity and Pore Morphology

During fabrication NPN can be created at varying porosities. However, membrane porosity is often linked with geometric nuances that can enhance or hinder membrane performance beyond number of pores available. More specifically, porosity is a function of etching time in the lithography process [2]. Higher porosity mem-

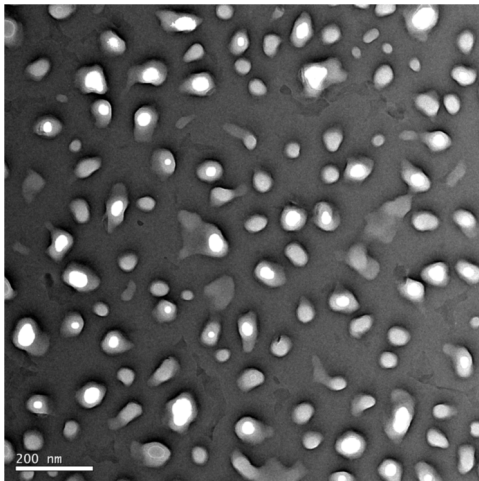


Figure 2.21: Low Porosity (2.7%)

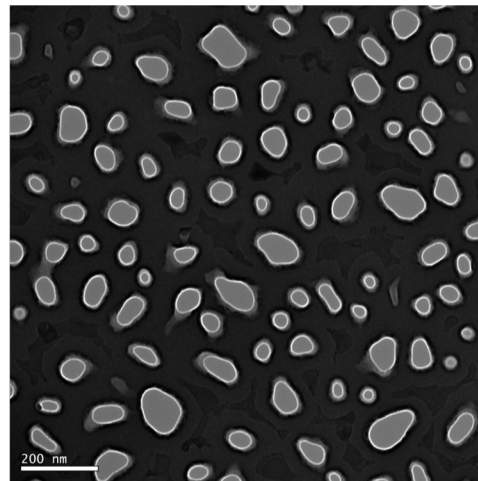


Figure 2.22: High Porosity (18.8%)

Figure 2.23: Geometric constructs in low porosity membranes such as "divots" and large pore orifices play an integral role in the reduced performance of these membranes. Higher porosity membranes have fully constructed pores with a slightly tapered geometry, improving their function overall.

branes tend to have fully developed pores with elliptical or circular shaped orifices and slightly tapered pore structure. Conversely, low porosity membranes present large and irregularly shaped orifices with a highly tapered "bowl-in-a-hole" or sink-like builds. Figures 2.21 and 2.22 depict TEM images of 2.7% and 18.8% porosity NPN respectively where such differences are clearly observed. We posit that higher orifice to pore surface area ratios provides more opportunities to form protein cake layers. Protein deposited on a divot-like surface regime will be difficult to clear by ultrafiltration and will ultimately provide a backbone for further protein deposition and cake layer building. Hence, by increasing membrane porosity we increase critical flux performance by avoiding fouling promoting geometric constructs. Note that this explanation is not relevant for TE membranes since the nature of their

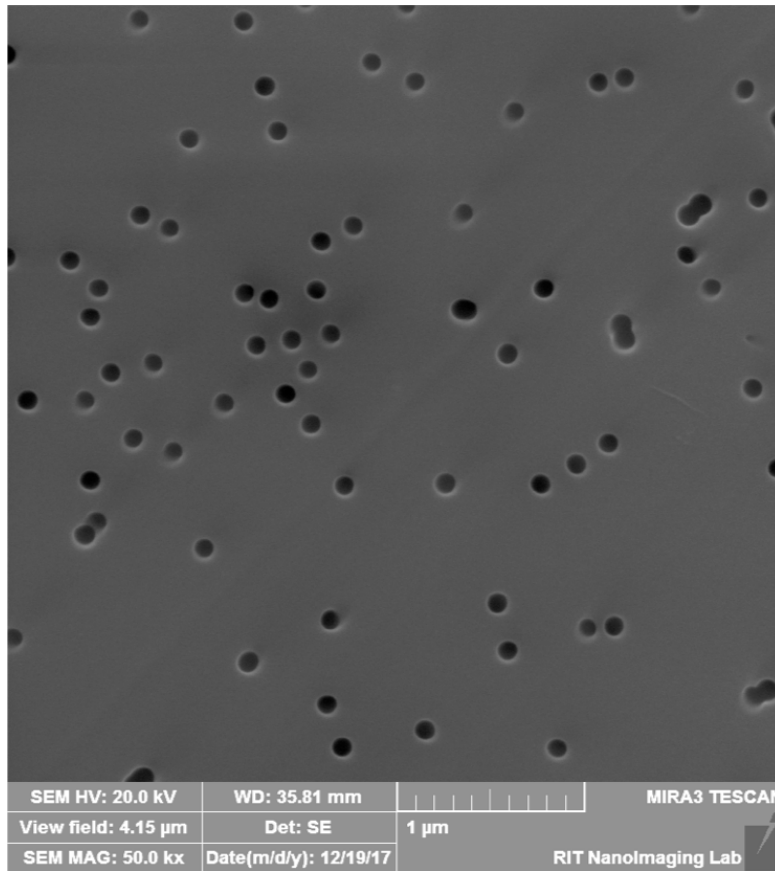


Figure 2.24: Track etched membranes are formed by irradiating a polymer surface with ions, leading to a consistent pore geometry. Image provided by Mehdi Dehghani (Rochester Institute of Technology).

manufacturing (ion irradiation) leads to pores with consistent geometry (Figure 2.24).

2.4.3 Parameter Sweep and NPN versus Track-Etched Membrane Performance

When varying protein concentration, 100 nm thick NPN is capable of dead end filtration up to a concentration of 10 mg/ml. This is in contrast to 10 μm thick TE membranes which are incapable of dead end filtration at 1 mg/ml BSA and fail to achieve critical flux at 30 and 60 mg/ml. At 10 mg/ml BSA, TE systems have an average $\frac{Q_u}{Q_s} < 0.1$. At 10mg/ml BSA concentration, we achieve an effective critical flux rate of 1157 LMH in NPN. This exceeds literature values for 1mg/ml BSA in 0.2 μm pore diameter TE membrane systems (220 LMH) [55] despite NPN pores being three times smaller. These TE membranes were much thicker (10 μm), requiring a higher TMP (Figure 2.15) to drive fluid through pores. We propose that a higher TMP lowers critical flux by increasing the chance of protein fouling on the membrane surface (Figure 1.5). This effect leads to degraded performance at higher concentrations, as seen in Figure 2.13. At higher transmembrane pressures, track etched membranes readily deform due to their polymeric structure. Indeed, the TE membranes were observed to visibly deform by bending downwards in experiments at supply rates $\geq 60 \mu\text{l}/\text{min}$, which were notable for high initial TMPs (Figure 2.18). This likely has the effect of reducing the diameter of pores on the membrane surface by making them more tapered.

Given these results, NPN offers a higher performance advantage versus TE membranes by maintaining lower transmembrane pressures. With this, we have shown that NPN can maintain a critical flux of $\frac{Q_u^*}{Q_s} = 0.367 \pm 0.033$ for 30 mg/ml

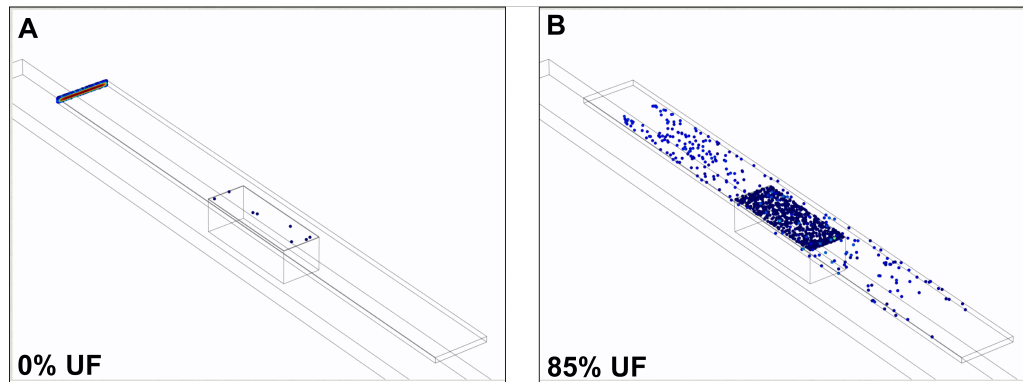


Figure 2.25: COMSOL modeling of particle capture in a TFF configuration (post run) shows particle deposition on a membrane surface with no set ultrafiltration (Panel A). A comparison with 85% ultrafiltration is shown in Panel B, where more particles deposit on the membrane. Simulation data from Kilean Lucas (University of Rochester).

protein concentration. This is valuable for blood plasma based diagnostics as undiluted plasma (60 mg/ml) will only need to be diluted by half before running this filtration process as part of an assay.

Functionally, increasing supply rate is designed to prevent formation of protein cakes by moving fluid quickly and mitigating the chance of protein deposition on the membrane surface by tangential flow only. Finite element analysis via COMSOL done by others in the McGrath lab has shown that tangential flow with no forced ultrafiltration can still deposit particles on a membrane surface, hence the rationale for increasing supply speed (Figure 2.25). The idea of "shearing" protein cakes is not the intended mechanic of study for this set of experiments. Indeed, with NPN increasing the supply rate provides a slight performance improvement in critical flux when comparing ultrafiltration rate only (Figure 2.12). However, critical flux ratios decrease as supply rates increases. The lack of critical flux improvement with increasing supply rate implies that "shearing" protein cakes is

not readily possible, and that laminar flow velocity at the membrane/fluid interface is insufficient for such clearing. Rather, ultrafiltration rate appears to be the primary driving mechanism in determining the critical flux value.

Given that critical flux rate decreases with an increasing supply rate, the explanation for NPN systems doesn't work for track etched systems. Figure 2.14 shows an inverse relationship between critical flux and supply rate, where performance decreases as supply rate increases. Pressure data in Figures 2.16 and 2.17 explains this phenomena. Note that the TMP at the start of an experiment is significantly higher for track etched systems versus NPN despite using thirty times less concentrated protein solution. As supply rate increases in track etched systems, this initial TMP increases as well. This simultaneously deforms the polymeric membrane surface and promotes the formation of protein cakes. Thus, the higher pressures in track etched systems are due to their increased membrane thickness which causes increased resistance to ultrafiltration. The rigidity of their acrylic support layer versus PDMS in NPN devices is also a potential factor. Regardless, our hypothesis has been validated as we see higher critical flux performance in NPN due to a lower thickness and TMP.

2.4.4 Gold Nanoparticle Capture and Critical Flux

Biofluids feature complexity with particles and many proteins. While multi-protein solutions were not examined in the course of this research, gold nanoparticles were used as a surrogate for exosomes and other small particles in blood. A "complex" protein solution was used in experiments featuring 1 mg/ml BSA and

gold nanoparticles of varying diameters. Initial experiments with 60nm gold particles have critical flux ratios as high as 0.5 despite particles size matching average pore diameter (Figure 2.18). Oversaturating the membrane still allowed for critical flux, meaning that fluid flow was still possible around particle obstructions. Image analysis of NPN membranes also found a few pores with ~ 100 nm diameter. The relationship between volumetric flow rate and pore size is non linear [56]. In NPN systems this means that the largest 20% of pores provide 50% of flow [57]. Hence, using 60nm particles alone is insufficient to block the membrane. Mixing 60nm and 100nm particles in 1mg/ml BSA at high concentrations negate the membranes ability to maintain critical flux overall. High resolution separation is depicted in Figure 2.19, where flowing 10^9 30nm gold particles had no effect on membrane critical flux. Results from these experiments show similar performance to dead end filtration.

3. Capacity of Microporous Membranes with Microparticle Contamination

3.1 Introduction

Operating membranes in various environments requires understanding parameters at which systems fail so that appropriate actions can be taken before such an event occurs. In particular, capacity is an important functional characteristic of membranes that defines the limit of use for fouling during separation processes. Note that the primary mode of fouling for ultrathin membranes is surface fouling due to their lack of internal structure compared to thicker membranes. With protein filtration, this means that membranes can act as sensors for fouling when TMP is monitored in TFF, as rapid increases in TMP mean that a protein cake is forming on the surface of the membrane. This is particularly useful in the production of biopharmaceutical products where there's a need to retain protein product from a complex biofluid background. Fouling reduces permeate flux and can potentially make a membrane non reusable, increasing the costs of production. If a process is stopped once a membrane reaches capacity, the membrane can be cleaned and

prepared for further use. Beyond cost, production of some of these therapeutics is strictly regulated where products that fail to reduce viral contamination below acceptable thresholds face rejection from regulatory bodies [24]. For example, in virus derived human or animal vaccines, viral remnants are an undesired product that need to be removed [58] and are commonly purified by membranes [34]. Thus, understanding membrane capacity in purification processes provides value to the filtration process by providing a means to monitor avoid and ensure higher throughput.

In addition to utility in bioprocess design, understanding the capacity of ultrathin silicon membranes could provide an approach to growing problem of microplastic contamination. Microplastic contamination is common across the planet [35]. Roughly 92% of all plastics produced are not biodegradable [35, 37] and ultimately break down into microplastics < 5 mm long [41]. Given that these plastics are common in consumer products [43] and have been shown to pass through the epithelia of simple aquatic organisms like Mussels [45], the implications for human health are worrying. Techniques for assessment and filtering of water samples are required for better analysis of the plastics problem. Using ultrathin membranes provides a rapid method of isolating plastics from water (Figure 3.1) and the optical transparency of these membranes enables imaging modalities and analytical techniques unavailable to conventional membrane sources. An understanding of membrane capacity is useful in this regard since flowing microplastic contaminated water onto a membrane surface can cause debris cake formations. By understanding membrane capacity we can avoid building up layers

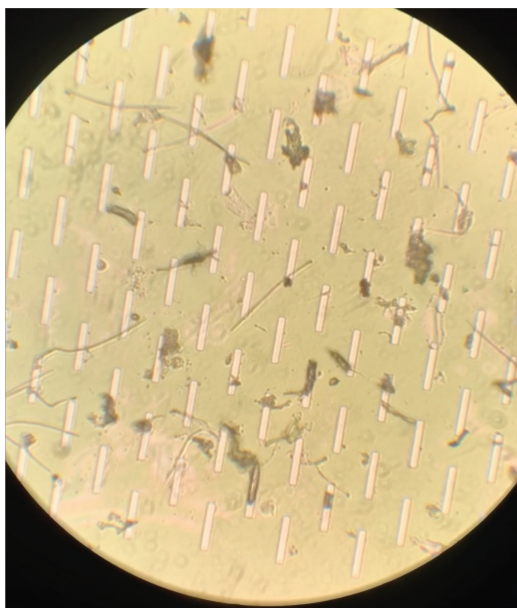


Figure 3.1: Microplastic contamination in drinking water from a water fountain. The membrane in the background consists of $8\ \mu\text{m}$ slits and features a variety of microplastics ranging from fibers to particulates.

of plastic debris on a membrane surface by ceasing flow when capacity is reached. This means that plastics on the membrane surface are visually identifiable and optical techniques such as Raman spectroscopy are applicable for analysis.

3.2 Materials and Methods

3.2.1 Microporous Membrane Device Manufacture

Microporous membrane microfluidic devices containing $8\ \mu\text{m}$ slit membranes or $3\ \mu\text{m}$ circular pore membranes were manufactured in the exact same way as NPN devices described in Chapter 2. Briefly, a $20 \times 40\ \text{mm}$ glass slide provided support

for a bottom channel gasket layer, and the rest of the device was assembled layer by layer with gasket and a PDMS top support. No changes in procedure were made in except for changing the type of chip being used. The dimensions of the microporous chip (5.4 x 5.4 mm) and the membrane window (0.7 x 2 mm) are also the same as the NPN chips used in Chapter 2.

3.2.2 Extended Length Membrane Device Fabrication

A limited number of devices featuring 0.5 μ m slit membranes that were twice as long (5.4 x 10.8 mm) as all other membrane chips used in this research were created. Accommodating this size increase required altering the dimensions of the microfluidic device since the membrane window also increased to 0.7 x 8.4 mm, and this was done in the craft cutter software. Each gasket layer was extended from 12 x 24 mm to 12 x 36 mm. The gasket layers were adjusted so that the chip gasket layer was large enough to accommodate the larger membrane chip and all other channels were extended as needed. Beyond an increase in length, no other changes were made to devices featuring these membranes.

3.2.3 Mathematical Modeling of Microporous Membrane Systems

A mathematical model was created in order to gain insight on microporous membrane system behavior while fouling. Specifically, the model calculated changes in resistivity and transmembrane pressure as the active membrane area experienced

occlusion from simulated rectangular particles. Rectangular particles are used to make calculations simple circular particles create more complex geometries when occluding the membrane surface. Resistivity and pressure can be calculated from adapting formulas from literature for rectangular channels [59]. The resistivity for flow in a rectangular channel is shown in Equation (3.2).

$$R_{hyd} = \Delta P / Q \quad (3.1)$$

$$R_{hyd} = \frac{12\eta L}{1 - 0.63 \frac{h}{w}} \frac{1}{h^3 w} \quad (3.2)$$

For the model we let s be an array with $n = 504$ elements such that $s = \{s_1, s_2, s_3, \dots, s_{504}\}$.

This was used to simulate the number of active slits on an $8 \mu\text{m}$ slit membrane with each $s_i \in s$ representing a slit on the membrane. We let l be the array $l = \{1, 2, 3, 4, 5\}$ and t be the array of permutations σ of l with $n = 504$ elements. The array l represents the possible absolute positions a $10 \mu\text{m}$ particle can take on $50 \mu\text{m}$ of space on a slit assuming even space distribution, no overlap, and no slipping. Thus, we note that all $t_i \in t$ have five elements. The array of permutations σ is specifically defined as:

$$\sigma = \begin{pmatrix} l_1 & l_2 & l_3 & l_4 & l_5 \\ \sigma(l_1) & \sigma(l_2) & \sigma(l_3) & \sigma(l_4) & \sigma(l_5) \end{pmatrix}$$

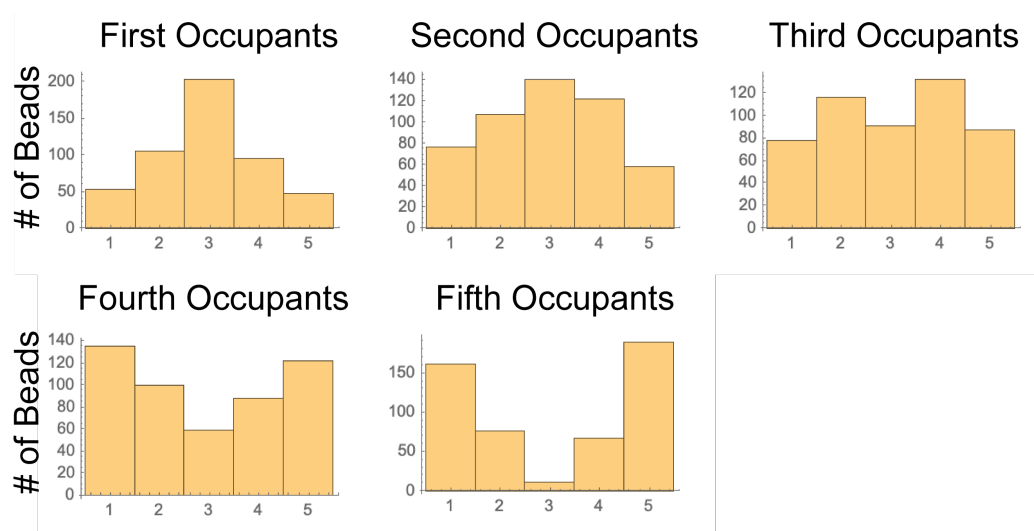


Figure 3.2: A series of histograms detailing which spot on all slits is occupied when each slit has a specific number of occupants.

A pseudo-random number sampling process utilizing a probability mass function was used to fill each element $s_i \in s$ with permutations $t_i \in t$ such that $f : t \rightarrow s$ is a one to one correspondence. Note that order matters and the highest probability for first member for any given t_i is 3. The probability mass function is as follows:

$$P_X(x) = \begin{cases} 0.1 & x = 1, 5 \\ 0.2 & x = 2, 4 \\ 0.4 & x = 3 \\ 0 & \textit{otherwise} \end{cases}$$

The order of any given member $s_i \in s$ dictates what order the particles land on that

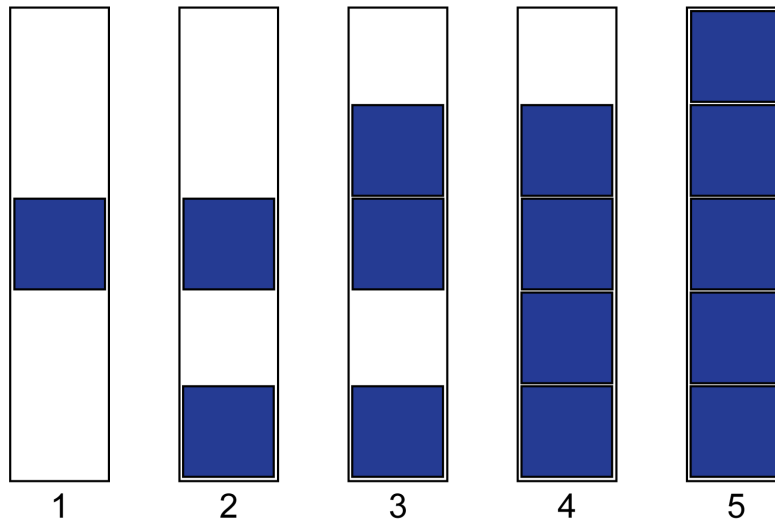


Figure 3.3: A diagram detailing an example of how a slit can be sequentially occupied in the model where $t_m = \{3, 5, 2, 4, 1\}$ (for an arbitrary m). Each time a particle lands the dimensions of the channel change, thus changing the resistivity of the slot. In order to avoid computational issues pertaining to $\frac{1}{0}$ errors, the particles used in this model were purposely made slightly smaller than the slit width.

specific slot. So we get that s is:

$$s = \{t_1, t_2, t_3 \dots t_{504}\}$$

An example of s could then be: $\{\{3, 1, 2, 4, 5\}, \{2, 3, 5, 4, 1\}, \{3, 2, 4, 1, 5\}, \dots\}$. The end result of the bead placement process is seen in Figure 3.2, where the order of each particle occupying a slit are shown. The first occupants of every slit follows the probability mass function closely but successive occupants deviate from that pattern as expected. Each time a particle lands on the membrane the resistivity of the membrane increases as parallel channels are added (Figure 3.3). In hydraulic

circuits, resistors in parallel are summed such that:

$$R_{tot} = R_1 + R_2 + R_3 + \dots + R_n$$

Let $r \in s_i$. For each $r \in s_i$ the resistivity of the slot is calculated based on the subsequent changes in slot dimension and stored in a separate array where five arrays (p_1, p_2, p_3, p_4, p_5) are generated. Each of these five arrays contains all resistivity calculations for a specific number of particles in slit. So p_1 is the array that contains all resistivity values for a single particle blocking a position on its respective slit, p_2 has all two particle resistivity calculations, and so on. Any p_i can be written as:

$$p_i = \{R_{hyd}(s_1(r_i)), R_{hyd}(s_2(r_i)), R_{hyd}(s_3(r_i)), \dots, R_{hyd}(s_{504}(r_i))\}$$

This also means that any $s_i = \{p_1(i), p_2(i), p_3(i), p_4(i), p_5(i)\}$. To account for time, the model takes an experimental flow rate (2 ml/min), fluid volume (50 ml), and assumes 2520 beads present in the solution. Note that 2520 beads is the maximum number of beads that can fill in 504 slits. Under these conditions beads land on the membrane at about 2 beads/s. A time array was then generated at 2 Hz with 2520 elements where $time = \{0, 0.5, 1, 1.5, \dots, 1260\}$. If faster flow rates are needed, the time array can be recalculated by finding the number beads impacting the surface of the membrane per second. Then beads/s is the frequency of the time array with a maximum of 2520 elements to control for number of beads. Since each p_i is the array that represents each slits resistivity with i particles blocking it, total resistivity

still needs to be calculated in a manner that matches the number of beads incident on the membrane (2 beads/s). To do so, p_1 is accumulated into a new array p_t such that $p_t = \{p_1(1), p_1(1) + p_1(2), p_1(1) + p_1(2) + p_1(3), \dots, p_1(1) + \dots + p_1(504)\}$. The accumulated array p_t now represents the total resistivity of the membrane with each slit experiencing one particle occlusion. Next $p_t + (p_2 - p_1)$ is added and appended to the array. Subtracting $p_2 - p_1$ provides the change in resistivity in all slits when a second particle is added and maintains the integrity of the order of any $s_i \in s$. Adding all of these Δ resistivities to each p_t in order now makes p_t the array that represents total membrane resistivity when all slits have two particles in them. Then $p_t + (p_3 - p_2)$ is added, and so on until all p_i have been appended in a similar manner. The arrays p_t and $time$ are designed so that they have the same length. They are subsequently transposed into a new array called *model* which maintains the condition of 2 beads/s. This array was then plotted and gives us resistivity over time. Resistivity was converted into pressure as well. The model was designed so that each run of the script produced a new simulation.

3.2.4 Polystyrene Bead Sample Preparation

Polystyrene bead solutions of various nominal diameters (10 μm , 3.4 μm , and 0.87 μm) from SpheroTech (Lake Forest, IL) were serially diluted in PBS and used for capacity experiments. Before dilution and experiments, the samples were vortexed and sonicated to ensure that the beads were homogeneously dispersed in solution and non aggregated.

3.2.5 Experimental Process and Data Collection

Data collection for this series of experiments used the same tangential flow setup as described in chapter 2 except the supply rate and ultrafiltration rates were matched. This results in a dead end filtration setup and no tangential flow will occur in the system at the start of an experiment. Preliminary dead end filtration experiments in a TFF setup have shown that fluid will leave the top outlet when a membrane becomes fouled. For experiments involving 8 micron slit membranes, parameters were set to match the mathematical model. $Q_s = Q_u = 2$ ml/min with 50 ml of 10 μm polystyrene bead laced PBS (loaded in a 60ml syringe). This results in a 25 minute runtime for these experiments. Pressure data was gathered in the exact same way as experiments in Chapter 2, where pressure sensors were placed in series with the fluid device channels. Data was similarly analyzed in script after collection. Experiments involving 3 μm pores had different flow rates, with $Q_s = Q_u = 0.4$ ml/min with 10 ml of 3.4 μm polystyrene bead laced PBS (loaded in a 10ml syringe). The runtime for these experiments was also 25 minutes. Lastly, experiments involving 0.5 μm slits had much slower flow rates, with $Q_s = Q_u = 0.1$ ml/min with 10 ml of 0.87 μm polystyrene bead laced PBS (loaded in a 10ml syringe). These experiments lasted for about an hour and forty minutes.

3.2.6 Video Recording of Capacity Experiments

Transmembrane pressure was recorded in the exact same way for these experiments as previously described in Chapter 2. The experimental setup with the pumps was

Membrane	0.5 μm	3 μm	8 μm
Bead Size	0.87 μm	3.4 μm	10 μm
Concentrations Run	100k	100k	2.8k, 5.7k, 28k, 280k
Dead-End Filtration Rate	0.1 $\mu\text{L}/\text{min}$	0.4 $\mu\text{L}/\text{min}$	2ml/min

Table 3.1: An overview of all experiments performed in this chapter. Each experiment was run in triplicate.

also the same, however a microscope and camera apparatus was utilized to record particles fouling a membrane in real time. Briefly, devices were placed in a microscope (BX51, Olympus Corporation, Tokyo, Japan) and a camera (D3300, Nikon Corporation, Tokyo, Japan) was attached to the right eye-piece. This allowed for recording of experiments in progress at high resolutions and frame rates. Experiments were recorded at various magnification levels depending on the type of microporous chip being used. Any experiment done on 8 μm slits were recorded at 5x objective and 3 μm circles were recorded at 40x objective. Experiments involving 0.5 μm membranes were not recorded.

3.2.7 Membrane Chip Analysis and Statistics

Pertinent information (such as slit dimensions and number of slits) about the 0.5 μm slit membranes were provided by the manufacturer of the membrane wafer. The 8 μm slit membranes and the 3 μm circle pore membranes had their characteristics verified with microscopy. Specifically, the camera microscope system mentioned earlier in this chapter was used to take images of the membranes. For the 8 μm slits a manual counting process was possible as a 5x objective lens was capable of providing a view of most of the membrane. For the 3 μm circle pore membranes a

40x lens was needed. Several pictures were taken and an approximate number of pores was calculated based on extrapolating the area of the frame to the area of the membrane and the number of pores present in a frame.

3.2.8 Definition of Capacity

The capacity of a membrane is the volume of a sample that can be processed before a significant rise in TMP occurs due to a decrease in permeability. Because we are maintaining constant flux in our experiments, a membrane has reached its limit when pressure rises, causing the system to fail. Thus for the purposes of this chapter we will define capacity in terms of the number of particles occupying a membrane when a steady and significant increase in TMP occurs. For the 10 μ m polystyrene bead experiments with 8 μ m slits, experiments using 2.8k and 5.7k total beads reached capacity when Δ TMP > 25% in 60 seconds. Note that this definition was also used for the 0.5 μ m slit experiments and 3 μ m circle pore membrane experiments since the number of particles in bead solution were in the same order of magnitude as number of available spots on the membrane surface. For higher bead concentrations on 8 μ m slit membranes the timescale of fouling was shorter so the definition of capacity was modified accordingly. Experiments featuring 28k 10 μ m beads reached capacity when Δ TMP > 25% in 20 seconds. The 8 μ m slit membrane experiments with 280k 10 μ m polystyrene beads fouled the membrane in less than 10 seconds, thus the capacity time taken for these experiments was when Δ TMP > 25% in 3 seconds. Table 3.2 details information about all microporous membranes used in this research. Occupancy will be normalized to the number of possible

	0.5μm	3μm	8μm
Pore Type	Slit	Circle	Slit
Bead Size	0.87 μm	3.4 μm	10 μm
Beads/Pore	55	1	5
Max Beads	90145	~100000	2520
Pore Density	278.7 slits/mm ²	71.4k pores/mm ²	360 slits/mm ²
Porosity	11%	32%	15.4%
Membrane Area	5.88 mm ²	1.4 mm ²	1.4 mm ²

Table 3.2: Information relating to capacity of membranes is depicted in this table. The row "Max Beads" is the definition of 100% occupancy. Membranes are capable of supporting an occupancy well beyond that number and can even remain permeable with robust bead cake formations on them. positions on a membrane a particle can occupy that results in visible occlusion of membrane space, although in practice membranes are capable of exceeding "total occupancy" and can still remain permeable despite robust fouling and evidence of bead "cake" formations.

3.3 Results

3.3.1 Mathematical Modeling of 8 μm Membranes

While each simulation run is unique due to the pseudo-random process that provides the order in which particles sequentially occupy slits, pressure data tends to be consistent due to the geometrically limited nature of the model. Figure 3.4 depicts a typical response in the model system. We note small increases in pressure are apparent while slits are being partially obstructed and a dramatic rise in pressure is noted at around 1000 seconds of runtime, which calculates to 80% occupancy. For

the $8\mu\text{m}$ slit membrane, this translates to roughly 2000 beads incident upon the membrane surface.

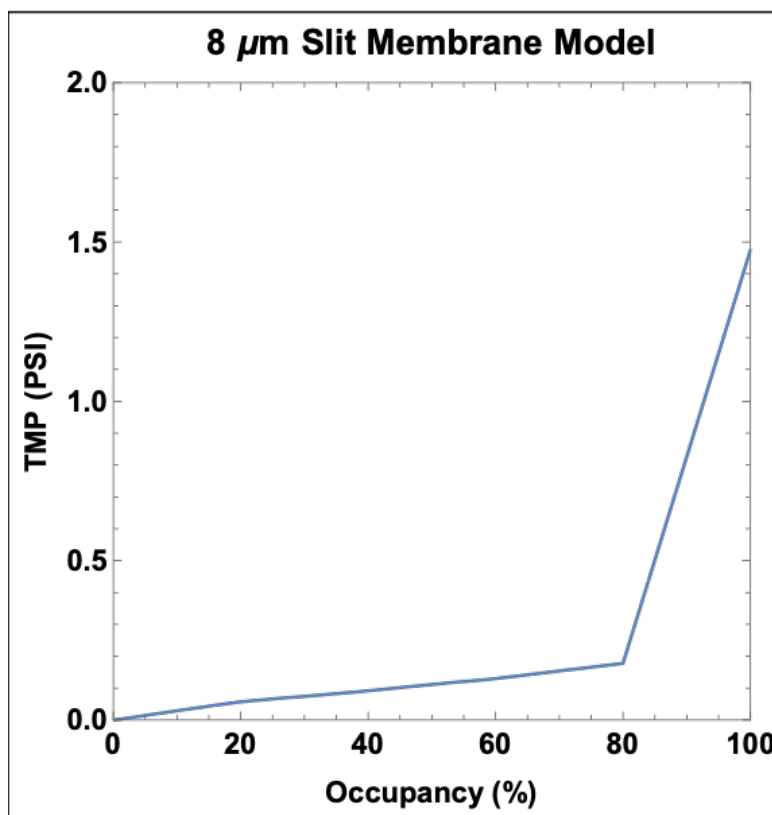


Figure 3.4: Initial pressure rises are marginal as particles accrue on the simulated membrane. This continues until about 80% capacity is reached (roughly 1000s), where we see an inflection point where pressure rises dramatically.

3.3.2 Experimental Results with $8\mu\text{m}$ Slit Membranes

A summary of the $8\mu\text{m}$ slit pore membrane bead experiments with $10\mu\text{m}$ polystyrene beads is detailed in Figures 3.8 and 3.9. Briefly, experiments conducted with low bead concentrations (2.8k beads in 50ml PBS) exhibited reduced perfor-

mance compared to the model, with capacity at $64.00 \pm 0.05\%$ occupancy with 1623 ± 136 beads at an average of 870 ± 73 seconds. Note that the pressure rise was more subtle across all experiments performed at this concentration, reaching an average maximum of 0.53 PSI at the end of an experiment. Figure 3.5 depicts key frames at 375 second time intervals from an experiment recording as well as corresponding pressure data. At a concentration of 5.7k beads per 50ml of PBS similar results occur with capacity at $52 \pm 10\%$ occupancy with 1317 ± 253 beads at an average of 329 ± 63 seconds. The 5.7k bead experiments had a more distinct pressure rise versus the 2.8k bead experiments (Figure 3.6). This trend continues as particle concentration increases with results from 28k bead experiments (Figure 3.7) showing capacity at $62.7 \pm 3.9\%$ occupancy with 1580 ± 98 beads at an average of 84.7 ± 5.2 seconds. The last set of experiments (280k beads) had capacity at $59.3 \pm 4.3\%$ occupancy with 1493 ± 108 beads at an average of 8.0 ± 0.6 seconds. A triplicate of experiments with $0.5\mu\text{m}$ membranes was performed with similar results (capacity of $65.0 \pm 1.5\%$).

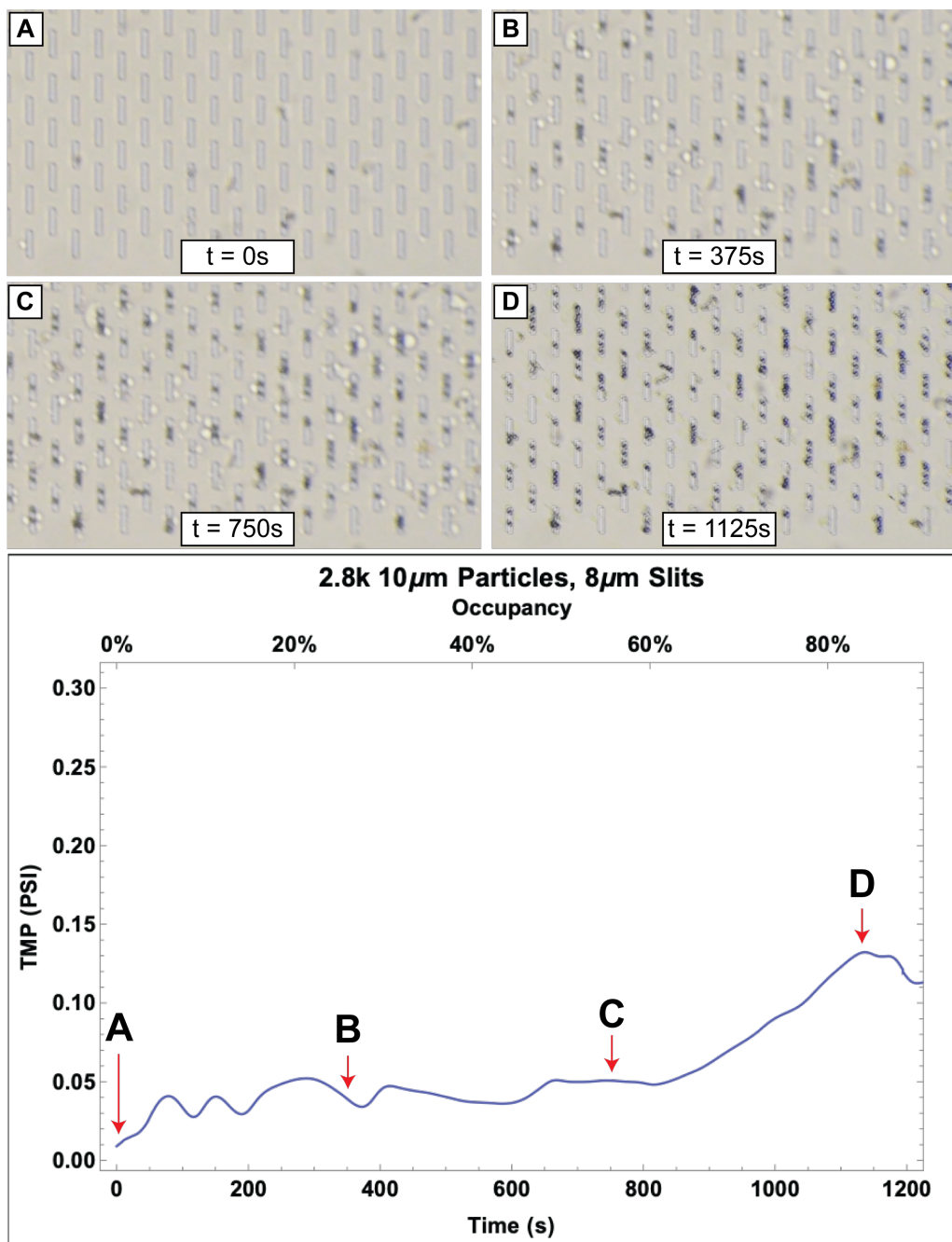


Figure 3.5: Frames over time taken from a recording of a ~ 2800 beads in 50ml PBS experiment. Pressure is stable despite concurrent fouling in the experiment until a critical amount of active membrane area is blocked. The resulting pressure rise is indicative of a membrane capacity, where maintaining flux requires a higher pressure driving force.

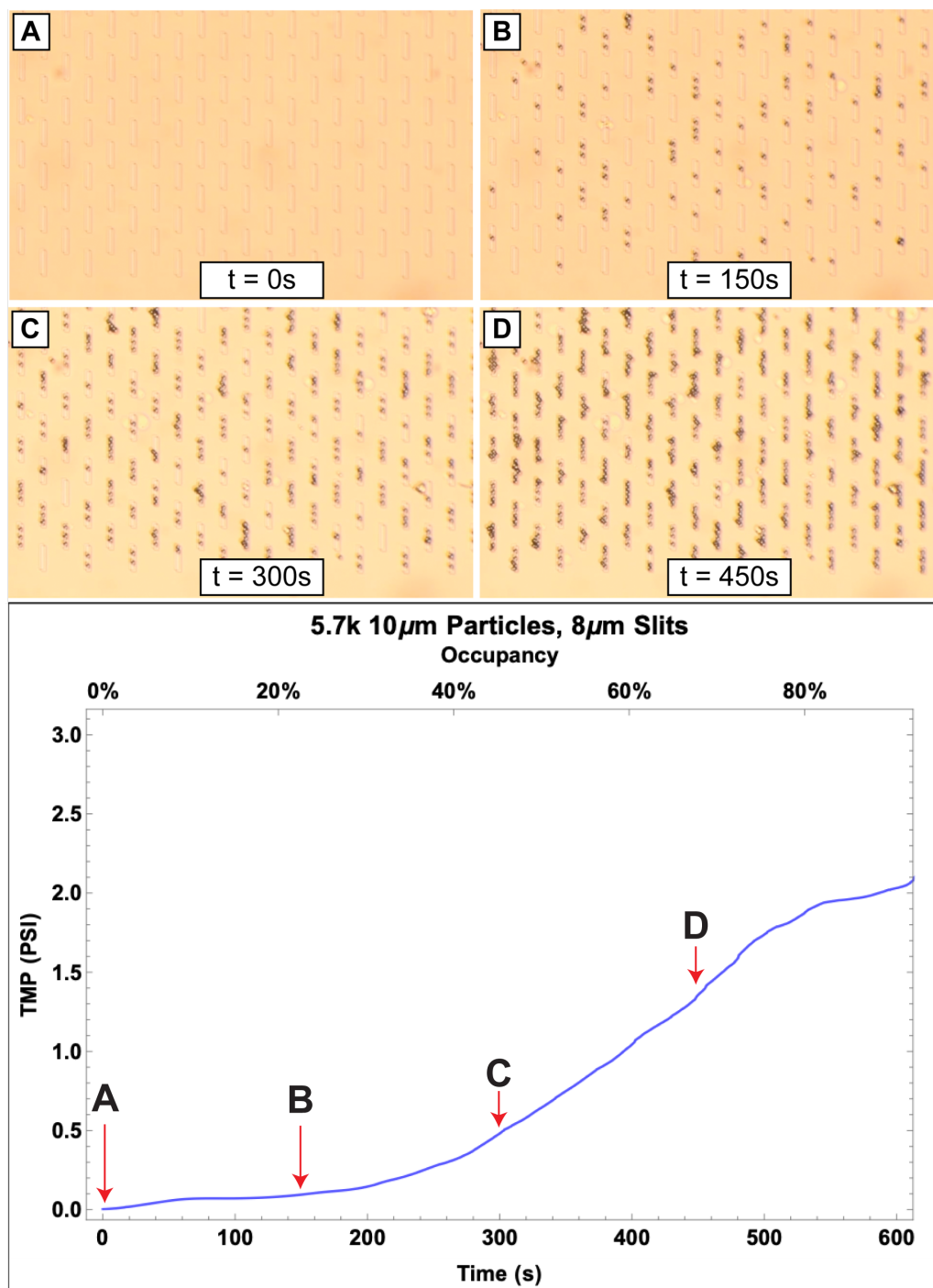


Figure 3.6: Frames over time taken from a recording of a ~ 5700 beads in 50ml PBS experiment. The timeframe for inflection occurs earlier than in 2.8k bead experiments.

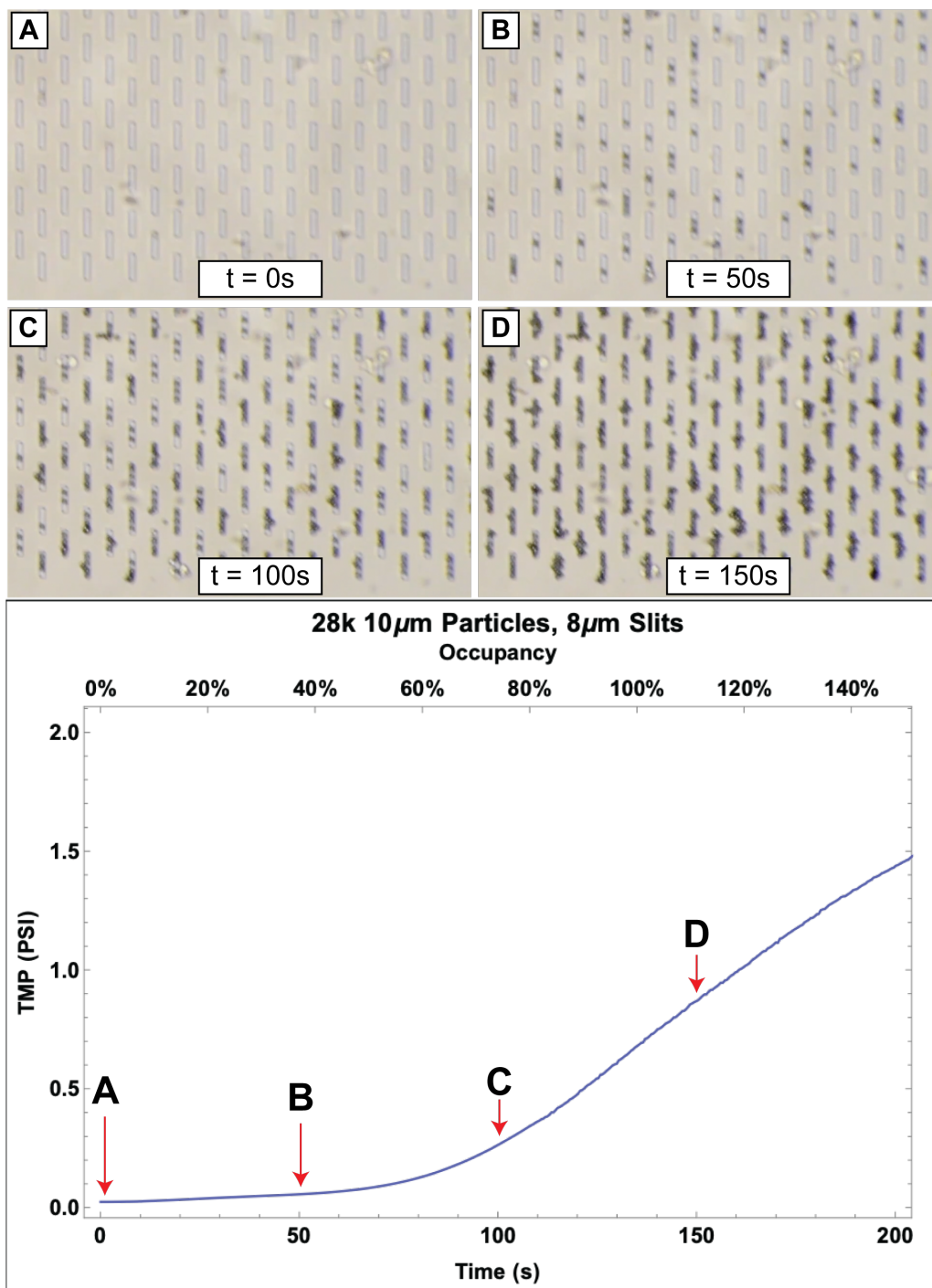


Figure 3.7: Frames over time taken from a recording of a ~ 28000 beads in 50ml PBS experiment.

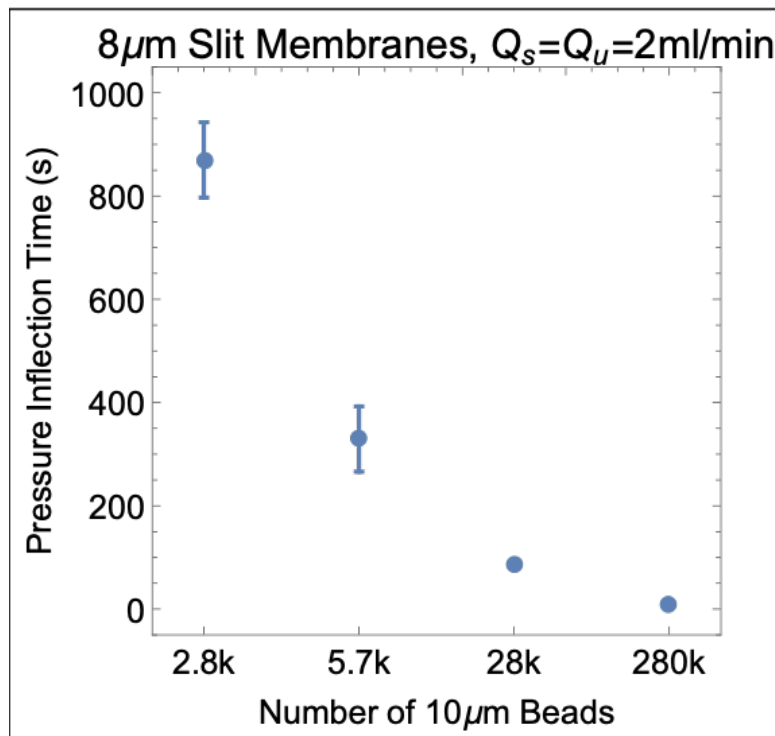


Figure 3.8: As bead concentration increases, pressure inflection points occur earlier in experiments. Increased bead distribution density corresponds to more robust pressure inflections as well as lower uncertainty between experiments.

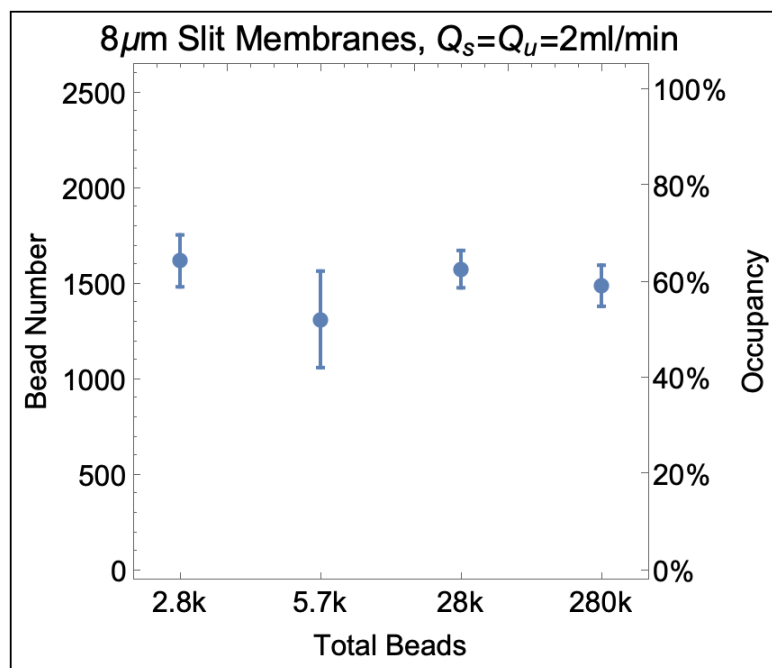


Figure 3.9: Across all experiments performed, pressure inflections tend to occur when $\sim 60\%$ of a membrane is occupied.

3.3.3 Experimental Results with 3 μm Circle Pore Membranes

Experiments with circular pore membranes were designed to match number of particles with number of pores as closely as possible. The 3 μm circle pore membranes have roughly 90k pores available and the 3.4 μm bead sample used in each experiment had $\sim 100\text{k}$ beads. Experimental flow rates were slower (0.4 ml/min) with a smaller volume passed (10 mL) compared to the 8 μm slit membrane experiments, however experiment times were matched (25 minutes). As seen in Figure 3.10, circular pore membranes started to experience a high pressure rise at $\sim 80\%$ capacity, matching the results seen in the mathematical model. More specifically, capacity was achieved at $80.51 \pm 0.05\%$ occupancy of the 3 μm circle pore membranes.

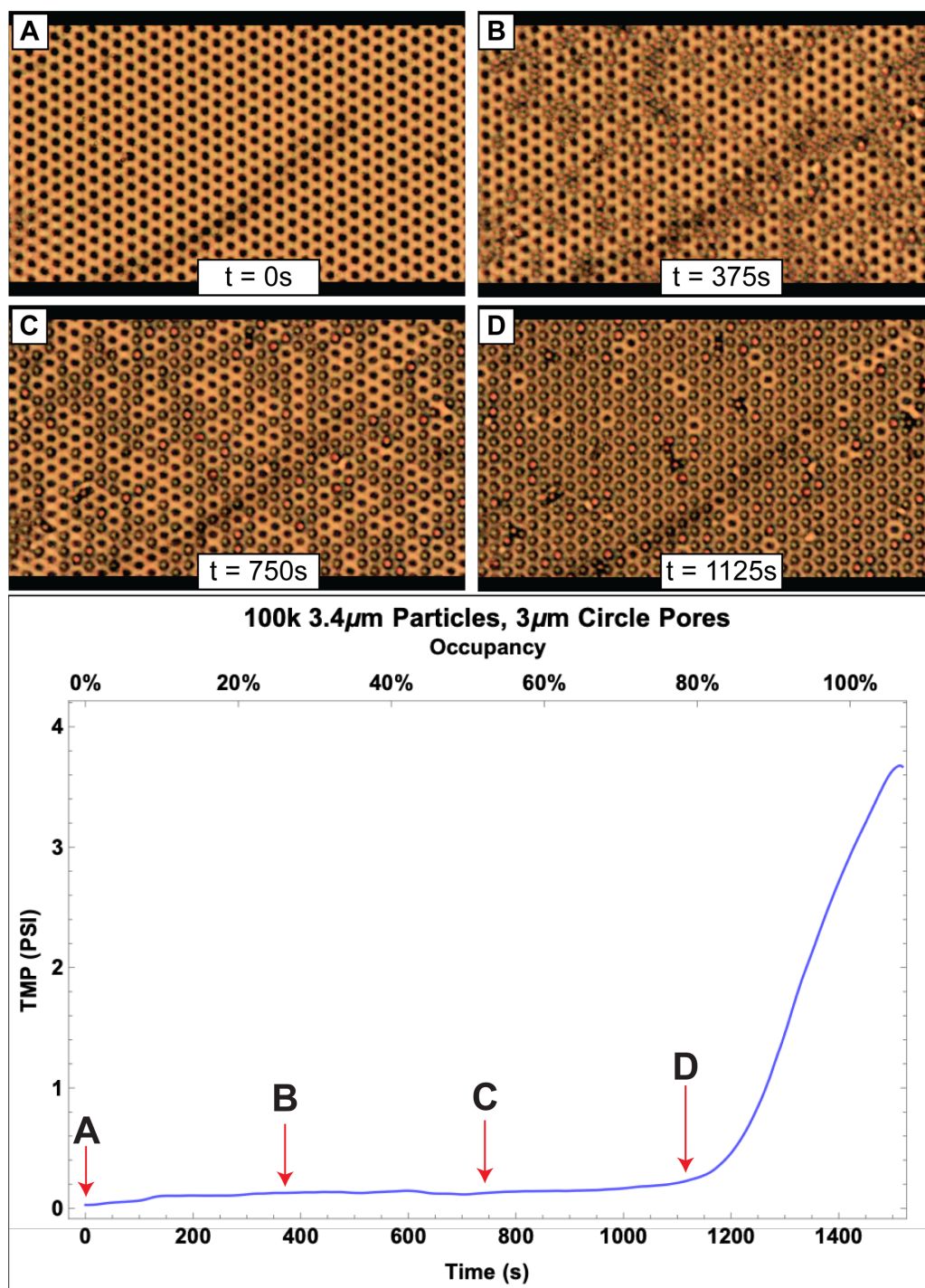


Figure 3.10: Frames over time taken from a recording of a ~100,000 beads in 10ml PBS experiment.

3.4 Discussion

In this chapter we assessed the capacity of ultrathin microporous membranes and compared the effects of pore geometry on TMP rise. A mathematical model designed to calculate change in resistivity over time due to particle capture in 8 μm slit membranes predicted a capacity of $\sim 80\%$ before a sharp rise in TMP. Experimental results with 0.5 and 8 μm slit membranes show lower performance with a capacity of $\sim 60\%$ while 3 μm circle pore membranes are capable of $\sim 80\%$ capacity. The following sections provide some additional perspective on these results and their implications.

3.4.1 Mathematical Modeling of Microporous Membrane Systems

The model presented in this research is designed to emulate an 8 μm slit membrane in dead end filtration of 10 μm polystyrene beads by first using elements in an array to represent slits in a membrane. Membrane resistivity is then iteratively calculated as beads impact the surface of the membrane and occupy slits. This is done by maintaining strict boundary conditions where only 5 particles are allowed to occupy a slit with no slipping or overlap. A volumetric flux rate of 2 ml/min is represented by calculating the number of beads impacting a membrane surface per second for a given amount of supply fluid and then subsequently generating a time array using beads/s as a frequency. Beads are distributed on the membrane surface through a pseudo-random process to mimic variability in bead placement in slits

during actual experiments.

Certain limitations exist for this model. First, using an array based model for probability calculations relies principally on geometric changes in the membrane system. This means that fluid dynamics are not being considered in any calculations which limits understanding how particles move into slits. While the model uses a pseudo-random process to mimic particle/slit interactions, context is lost in the form of streamlines that particles follow and path of least resistances as area is occluded on the membrane surface. Furthermore, the pseudo-random process for bead placement fills slits sequentially with particles one at a time. This means that each slit must have n occupants before another slit can receive its $n+1$ occupant. In contrast, some slits in experiments were observed to be fully occupied while others had no beads in them. Particle geometry is also simplified into rectangles and particles are incapable of slipping or filing "between spots", despite video evidence displaying both of these behaviors. One point to note, however, is that changes in resistivity in a slot when particles are occluding it are in the same order of magnitude until $\sim 80\%$ occlusion is reached. This suggests that particle slipping or overlap would have marginal effects on membrane resistivity and transmembrane pressure overall. Given these limitations, the model works as an overall guide and can benefit from more refinement.

Alternative techniques to model $8 \mu\text{m}$ slit membrane in dead end filtration of $10 \mu\text{m}$ polystyrene beads are possible, namely simulations via COMSOL. While COMSOL has significantly more options for analysis and can quantitatively assess fluid dynamics within membrane systems, particle capture simulations in COMSOL

lack the the ability to iteratively calculate membrane resistance as particles land and adjust membrane resistivity accordingly. Instead, COMSOL calculates streamlines first and has particles follow them until they're trapped on the membrane surface in one step. This work's model is capable of iteratively calculating membrane resistivity as particles occlude the membrane surface, making it more useful over COMSOL for our current purpose despite its simplicity.

3.4.2 Differences in Model and Experimental Results

A surprising conclusion from this chapter is that slit based membranes ($0.5\ \mu\text{m}$ and $8\ \mu\text{m}$) have a lower ($\sim 60\%$) capacity versus $3\ \mu\text{m}$ circle pore membranes ($\sim 80\%$) and that circle pore membrane results match closely with the slit membrane model. One possible explanation for this discrepancy may lie in the porosity of the membranes used. The $0.5\ \mu\text{m}$ and $8\ \mu\text{m}$ slit based membranes have porosities of 11% and 1.44% respectively, which is much lower than the 32% porosity of the hex-patterned circle pore membranes. For circle pore membranes, this results in a lower resistance for transmembrane flux and a subsequently higher capacity due to the increased number of locations for particles to occupy. We note, however, that the $3\ \mu\text{m}$ membrane experiments were designed as analogues to the low concentration $8\ \mu\text{m}$ slit experiments. This means that number of particles were closely matched to number of available pores, controlling for porosity. The $8\ \mu\text{m}$ membranes experienced a small linear rise in transmembrane pressure upon reaching capacity while the $3\ \mu\text{m}$ membranes experienced rapid pressure rise similar to the model. The lower TMPs in slit membranes can be attributed to higher permeability at

100% occupancy versus the total occlusion experienced by circle pore membranes at 100% occupancy. Furthermore, experiments show that slit membranes will remain permeable despite the formation of "bead cake" layers. This suggests that transmembrane flow is still easily accessible in slit membranes despite blockages due to the rectangular geometry of the slits while circular membranes experience total occlusion and rapidly lose permeability during an experiment.

3.4.3 Analytical Tools for Microplastics Analysis

Plastic pollution is ubiquitous across the environment with over 79% of all plastic ever made (~ 4977 Mt) currently sitting in landfill environments [35]. The overwhelming majority ($\sim 92\%$ [35]) are not biodegradable [37] and will ultimately decay into micro and nanoscale sized plastics [40]. Given this, accurate tools are needed for microplastics assessment and recovery. Ultrathin membranes have a number of properties that serve this purpose, namely optical transparency and fabrication with non-plastic components. While the studies conducted in this chapter used simple microscopy to record membranes undergoing particle capacity experiments, the unique nature of these membranes allows for enhanced interrogative techniques such as spectroscopy and fluorescent marking. Future work involving plastic characterizations is readily accessible through the usage of this membrane technology and understanding of capacity.

3.4.4 Membranes as Sensors for Bioprocessing

A common use of membrane technology is purification of viruses from biopharmaceutical products. This process needs precision, as regulatory bodies will reject a product for clinical trials if it fails to meet purity criteria [24]. Furthermore, viruses are purified from protein rich environments which runs the risk of irreversible fouling if membranes are not monitored properly [34]. Standard protocol for membrane use with virus purification also involves washing and re-using membranes [34], increasing the need for inline monitoring processes to ensure that irreversible fouling is not occurring. Membranes in this research show significant TMP rise when fouling above a threshold. This mechanism makes these ultrathin membranes potentially as a sensor for fouling, since there are negligible changes in TMP before a fouling threshold is reached. Thus, these membranes can be utilized in the purification process both for both filtration and as a sensor for fouling.

4. Summary and Future Directions

4.1 Summary

4.1.1 Optimizing Critical Flux of Ultrathin NPN

Critical flux is the transmembrane flux below which a membrane based microfluidic system experiences no fouling/flux decline with stable TMP and permeate flux [23]. This work has demonstrated that enhancing critical flux in NPN based microfluidic systems can be achieved by assessing protein aggregates, membrane porosity, protein concentration, and feed supply flow rate. Compared to TE microfluidic systems, NPN has lower TMPs and this promotes the formation of flowing protein cakes while higher TMPs in TE systems drives protein to a membrane surface and causing fouling.

Aggregates and denatured proteins act as building sites for further protein deposition [54]. Thus, removing protein aggregates from a BSA protein feed solution prevents opportunistic fouling from accumulation of protein aggregates on the top surface of a membrane [53]. Centrifuged 1 mg/ml BSA protein samples were verified for concentration (Figures 2.4 and 2.5) operated in a TFF flow mode ($Q_s =$

30 $\mu\text{L}/\text{min}$, $Q_u = 10 \% Q_s$ every 45 minutes) with NPN achieved critical flux in low porosity (2.7%) NPN membranes while unprocessed BSA rapidly fouled the 2.7% porosity NPN membrane at the lowest ultrafiltration ratio utilized (Figure 2.8). TMP regimes in the processed 1 mg/ml BSA sample were stable and twice as high as control experiments conducted with PBS.

Membrane porosity contributed significantly to NPN critical flux in experiments involving centrifuged 1 mg/ml BSA ($Q_s = 30 \mu\text{L}/\text{min}$, $Q_u = 10 \% Q_s$ every 45 minutes). Increasing NPN porosity from 2.7% to 18.8% resulted in a critical flux ratio $\frac{Q_u^*}{Q_s}$ increase from ~ 0.3 to ~ 1.0 with lower TMPs (Figure 2.9), meaning that the 18.8% porosity NPN was capable of dead end filtration of 1 mg/ml BSA (Figure 2.10). Transmission electron microscopy of the 2.7% and 18.8% membranes revealed geometric differences between pore construction explaining this phenomena (Figures 2.21 and 2.22). The 2.7% membranes presented high orifice to pore surface area ratios while the 18.8% membranes presented pores that were fully developed. A higher orifice to pore surface area ratio means that protein can get trapped in the orifice during ultrafiltration and tangential flow is unable to clear it, leading to more protein fouling and a subsequently lower critical flux.

Increasing protein serum concentration in NPN experiments from 1 to 60 mg/ml ($Q_s = 30 \mu\text{L}/\text{min}$, $Q_u = 10 \% Q_s$ every 45 minutes) resulted in dead end filtration up to 10 mg/ml BSA. Filtration of 30 mg/ml BSA was the first protein concentration at which a tangential component was required to mitigate fouling and promote critical flux with $\frac{Q_u^*}{Q_s} = 0.367 \pm 0.033$. Results at 60 mg/ml BSA were lower with $\frac{Q_u^*}{Q_s} = 0.200 \pm 0.058$ (Figure 2.11). A critical flux at 30 mg/ml

is significant, however, as this mean that physiological assays involving human plasma (60 mg/ml) would only need to be diluted by half before assessment.

Increasing supply rate initially gave modest improvements in critical flux performance with 30 mg/ml BSA and Q_u increasing by 3 $\mu\text{L}/\text{min}$ every 45 minutes. Going from $Q_s = 15$ to 30 $\mu\text{L}/\text{min}$ resulted in a 120% increase in critical flux ultrafiltration rate while going from 30 to 60 $\mu\text{L}/\text{min}$ resulted in a 27% increase. Any further increases in supply rate were met with no change in critical flux ultrafiltration rate and decreased critical flux ratios (Figure 2.12). Thus, we found that a supply rate of 30 $\mu\text{L}/\text{min}$ was optimal for 18.8% porosity NPN microfluidic systems since the critical flux ratio was highest, resulting in less sample loss with the experimental setup.

4.1.2 Comparing NPN and TE Critical Flux

Membrane devices made with TE membranes have a similar number of pores ($\sim 5 \times 10^7$ pores) and pore diameter (50 nm in TE vs 60 nm in NPN) to 18.8% NPN. The active areas were different, with the TE membranes having 2 mm^2 and NPN having 1.4 mm^2 . The TE membranes had a higher resistivity than NPN since TE membranes were 10 μm thick versus 100 nm thick for NPN. We hypothesized that higher TMP would drive protein to the surface of a thicker membrane, resulting in worse membrane performance due to fouling. Protein concentration and supply flow rate critical flux experiments were performed for TE membranes and compared against NPN results.

Protein concentration experiments in TE membranes with 1 mg/ml BSA

($Q_s = 30 \mu\text{L}/\text{min}$, $Q_u = 10 \% Q_s$ every 15 minutes) resulted in $\frac{Q_u^*}{Q_s} = 0.433 \pm 0.067$, which was lower than the performance of NPN with 1 mg/ml BSA ($\frac{Q_u^*}{Q_s} \sim 1$). TE membranes were only able to achieve critical flux up to 10 mg/ml BSA concentration (Figure 2.13), with significantly higher TMPs than NPN experiments (Figure 2.15). Noting these results, we have context for how TMP degrades thicker membrane performance with more concentrated protein solution.

Supply rate concentration experiments with TE membranes (1 mg/ml BSA, Q_u increasing by $3 \mu\text{L}/\text{min}$ every 45 minutes) had a critical flux performance advantage at $Q_s = 15 \mu\text{L}/\text{min}$ over NPN (at 30 mg/ml) with $\frac{Q_u^*}{Q_s} = 0.867 \pm 0.067$. Subsequent experiments show lowered critical flux rate performance (Figure 2.14), which is chiefly due to higher TMP as supply rate increases (Figures 2.16 and 2.17). Given these results, we note that higher TMPs in thicker membranes lead to degraded performance at faster supply rates.

4.1.3 Gold Particle Capture

The presence of particulate in complex biofluids was modeled by mixing 1 mg/ml BSA with gold nanoparticles and using the mixed solution in TFF experiments with 18.8% porosity membranes. The 18.8% NPN had an average pore size of about 60 nm, so 60 nm gold particles were used first and yielded critical flux capability at all particle concentrations assessed (10^7 , 10^8 , 10^9) (Figure 2.18). We noted that relationship between volumetric flow rate and pore size is non-linear [56], meaning that 20% of the largest pores accommodate 50% of flow through a membrane [57]. NPN membranes at 18.8% porosity feature pores as large as 100 nm, thus

using 60 nm particles only was insufficient for blocking them and 100 nm particles were added into the 1 mg/ml BSA solution. This resulted in no critical flux at high bead concentrations (10^8 , 10^9) (Figure 2.18). Having a high concentration of particles is shown to have no effect on critical flux if the particles are smaller than the NPN pore diameter (Figure 2.19), so they simply pass through. Ultrathin membranes lack internal structure, meaning that there is no means of accumulating small particles in the membrane space and surface fouling mechanisms are the primary driving force of fouling.

4.1.4 Mathematical Modeling of 8 μm Slit Membrane Capacity

The mathematical model created for analyzing resistivity changes in 8 μm slit membranes calculated membrane resistivity as simulated particle blocking was occurring. The simulated particles were rectangular and were designed to mimic 10 μm spherical polystyrene particles. A key understanding taken from that model was that slit membrane resistivity experiences negligible changes before 80% capacity is reached on the membrane surface (Figure 3.4). After 80% capacity, resistivity and TMP rise dramatically.

4.1.5 8 μm Slit Membrane and 3 μm Circle Pore Experimental Results

The 8 μm slit membrane experiments were designed with different concentrations, as such the timescale of achieving capacity is faster as bead concentration increases (Figure 3.8). The capacity results for the 8 μm slit membrane experiments are different from the results of the model, with roughly $\sim 60\%$ capacity in experiments versus 80% in the model (Figure 3.9). Key frames and pressure/capacity graphs from 2.8k, 5.7k, and 28k 10 μm polystyrene bead experiments on 8 μm slit membranes are detailed in Figures 3.5, 3.6, and 3.7. The 3 μm circle pore membranes had results closer to the mathematical model, with a capacity of $\sim 80\%$ (Figure 3.10).

4.2 Future Directions

4.2.1 Analyzing Biofluids in TFF

Albumin constitutes between 50 to 60 percent of the protein content found in human blood plasma [60]. The critical flux experiments performed in Chapter 2 with NPN and gold particle capture only used albumin, which lacks physiological context due to the omission of other plasma proteins. Given that these experiments are motivated by early cancer detection through exosome capture from plasma and urine, complex biofluids need to be analyzed in the lens of capture experiments that are motivated by the critical flux results obtained in this research. To this end,

analyzing the critical flux properties of NPN in TFF of diluted plasma solutions is necessary as a step to improve the TFF and exosome capture process for diagnostic medicine. This work established that 30 mg/ml BSA can flow through NPN with a tangential component in TFF. Thus, any experiments conducted will use half diluted plasma at 30 mg/ml protein concentration flown at similar regimes ($Q_s=30\mu l/min$ and $Q_u=10\% Q_s$ every 45 minutes) and will seek to address both critical flux and capture efficiency.

4.2.2 Assessment of Functionalized Membrane Surfaces

Surface fouling of NPN membranes by BSA in TFF is a pressure driven process, where TMP drives protein to the membrane surface where fouling can occur. Functionalization of the NPN membrane surface needs to be assessed as a means of fouling mitigation. Polyethylene glycol (PEG) coated membranes may enhance critical flux in NPN by preventing protein cake formation. Indeed, PEG (in conjunction with other compounds) has been used in literature to create "fouling resistant" membranes [61]. High concentrations of BSA (30 and 60 mg/ml) will be used since these two concentrations required a tangential component for filtration. Flow regimes will mimic the regimes previously used ($Q_s=30\mu l/min$ and $Q_u=10\% Q_s$ every 45 minutes) and changes in critical flux will be analyzed.

Bibliography

- [1] Striemer CC, Gaborski TR, McGrath JL, Fauchet PM. Charge- and size-based separation of macromolecules using ultrathin silicon membranes. *Nature*. 2007 02;445:749 EP –. Available from: <https://doi.org/10.1038/nature05532>.
- [2] DesOrmeaux JPS, Winans JD, Wayson SE, Gaborski TR, Khire TS, Striemer CC, et al. Nanoporous silicon nitride membranes fabricated from porous nanocrystalline silicon templates. *Nanoscale*. 2014;6:10798–10805. Available from: <http://dx.doi.org/10.1039/C4NR03070B>.
- [3] Dehghani MA, Lucas K, Flax J, McGrath J, Gaborski T. Tangential flow microfluidics for the capture and release of nanoparticles and extracellular vesicles on conventional and ultrathin membranes. 2019 06;.
- [4] Gaborski TR, Snyder JL, Striemer CC, Fang DZ, Hoffman M, Fauchet PM, et al. High-Performance Separation of Nanoparticles with Ultrathin Porous Nanocrystalline Silicon Membranes. *ACS Nano*. 2010;4(11):6973–6981. PMID: 21043434. Available from: <https://doi.org/10.1021/nn102064c>.
- [5] Johnson DG, Khire TS, Lyubarskaya YL, Smith KJP, Desormeaux JPS, Taylor JG, et al. Ultrathin silicon membranes for wearable dialysis. *Adv Chronic Kidney Dis*. 2013 11;20(6):508–515.
- [6] Briggs K, Madejski G, Magill M, Kastritis K, de Haan HW, McGrath JL, et al. DNA Translocations through Nanopores under Nanoscale Preconfinement. *Nano Lett*. 2018 2;18(2):660–668.
- [7] Agrawal AA, Nehilla BJ, Reisig KV, Gaborski TR, Fang DZ, Striemer CC, et al. Porous nanocrystalline silicon membranes as highly permeable and

- molecularly thin substrates for cell culture. *Biomaterials*. 2010 7;31(20):5408–5417.
- [8] Salminen AT, Zhang J, Madejski GR, Khire TS, Waugh RE, McGrath JL, et al. Ultrathin Dual-Scale Nano- and Microporous Membranes for Vascular Transmigration Models. *Small*. 2019 2;15(6):e1804111.
- [9] van Niel G, D'Angelo G, Raposo G. Shedding light on the cell biology of extracellular vesicles. *Nature Reviews Molecular Cell Biology*. 2018 01;19:213 EP –. Available from: <https://doi.org/10.1038/nrm.2017.125>.
- [10] Rajagopal C, Harikumar KB. The Origin and Functions of Exosomes in Cancer. *Front Oncol*. 2018;8:66.
- [11] Gallo A, Tandon M, Alevizos I, Illei GG. The majority of microRNAs detectable in serum and saliva is concentrated in exosomes. *PLoS One*. 2012;7(3):e30679.
- [12] Fernando MR, Jiang C, Krzyzanowski GD, Ryan WL. New evidence that a large proportion of human blood plasma cell-free DNA is localized in exosomes. *PLoS One*. 2017;12(8):e0183915.
- [13] Li M, Zeringer E, Barta T, Schageman J, Cheng A, Vlassov AV. Analysis of the RNA content of the exosomes derived from blood serum and urine and its potential as biomarkers. *Philos Trans R Soc Lond B Biol Sci*. 2014 Sep;369(1652).
- [14] Lee YS, Dutta A. MicroRNAs in cancer. *Annu Rev Pathol*. 2009;4:199–227.
- [15] van Reis R, Zydney A. Membrane separations in biotechnology. *Current Opinion in Biotechnology*. 2001;12(2):208 – 211. Available from: <http://www.sciencedirect.com/science/article/pii/S0958166900002019>.
- [16] Charcosset C. Membrane processes in biotechnology: An overview. *Biotechnology Advances*. 2006;24(5):482 – 492. Available from: <http://www.sciencedirect.com/science/article/pii/S0734975006000425>.

- [17] Scott K. MICROFILTRATION. In: Scott K, editor. Handbook of Industrial Membranes. Amsterdam: Elsevier Science; 1995. p. 373 – 429. Available from: <http://www.sciencedirect.com/science/article/pii/B9781856172332500106>.
- [18] Singh R. Chapter 1 - Introduction to Membrane Technology. In: Singh R, editor. Membrane Technology and Engineering for Water Purification (Second Edition). second edition ed. Oxford: Butterworth-Heinemann; 2015. p. 1 – 80. Available from: <http://www.sciencedirect.com/science/article/pii/B978044463362000001X>.
- [19] Belfort G, Davis RH, Zydney AL. The behavior of suspensions and macromolecular solutions in crossflow microfiltration. Journal of Membrane Science. 1994;96(1):1 – 58. Available from: <http://www.sciencedirect.com/science/article/pii/0376738894001197>.
- [20] Ghosh R. Rapid antibody screening by membrane chromatographic immunoassay technique. J Chromatogr B Analyt Technol Biomed Life Sci. 2006 11;844(1):163–167.
- [21] Christy C, Adams G, Kuriyel R, Bolton G, Seilly A. High-performance tangential flow filtration: a highly selective membrane separation process. Desalination. 2002;144(1):133 – 136. Available from: <http://www.sciencedirect.com/science/article/pii/S0011916402003016>.
- [22] Kurnik RT, Yu AW, Blank GS, Burton AR, Smith D, Athalye AM, et al. Buffer exchange using size exclusion chromatography, countercurrent dialysis, and tangential flow filtration: Models, development, and industrial application. Biotechnol Bioeng. 1995 Jan;45(2):149–157.
- [23] Field RW, Wu D, Howell JA, Gupta BB. Critical flux concept for microfiltration fouling. Journal of Membrane Science. 1995;100(3):259 – 272. Available from: <http://www.sciencedirect.com/science/article/pii/037673889400265Z>.
- [24] Huang PY, Peterson J. Scaleup and virus clearance studies on virus filtration in monoclonal antibody manufacture. Wang WK, editor. Boca Raton: CRC Press; 2001.

- [25] Roberts PL. Virus elimination during the purification of monoclonal antibodies by column chromatography and additional steps. *Biotechnol Prog.* 2014 11;30(6):1341–1347.
- [26] Victoria JG, Wang C, Jones MS, Jaing C, McLoughlin K, Gardner S, et al. Viral nucleic acids in live-attenuated vaccines: detection of minority variants and an adventitious virus. *J Virol.* 2010 6;84(12):6033–6040.
- [27] Victoria JG, Wang C, Jones MS, Jaing C, McLoughlin K, Gardner S, et al. Viral Nucleic Acids in Live-Attenuated Vaccines: Detection of Minority Variants and an Adventitious Virus. *Journal of Virology.* 2010;84(12):6033–6040. Available from: <https://jvi.asm.org/content/84/12/6033>.
- [28] Grzenia DL, Carlson JO, Wickramasinghe SR. Tangential flow filtration for virus purification. *Journal of Membrane Science.* 2008;321(2):373 – 380. Available from: <http://www.sciencedirect.com/science/article/pii/S0376738808004626>.
- [29] Lyddiatt A, O’Sullivan DA. Biochemical recovery and purification of gene therapy vectors. *Current Opinion in Biotechnology.* 1998;9(2):177 – 185. Available from: <http://www.sciencedirect.com/science/article/pii/S0958166998801122>.
- [30] Gias E, Nielsen SU, Morgan LAF, Toms GL. Purification of human respiratory syncytial virus by ultracentrifugation in iodixanol density gradient. *J Virol Methods.* 2008 2;147(2):328–332.
- [31] Jensen SM, Nguyen CT, Jewett JC. A gradient-free method for the purification of infective dengue virus for protein-level investigations. *J Virol Methods.* 2016 9;235:125–130.
- [32] van Reis R, Zydney A. Bioprocess membrane technology. *Journal of Membrane Science.* 2007;297(1):16 – 50. Available from: <http://www.sciencedirect.com/science/article/pii/S0376738807001159>.
- [33] Morenweiser R. Downstream processing of viral vectors and vaccines. *Gene Therapy.* 2005;12(1):S103–S110. Available from: <https://doi.org/10.1038/sj.gt.3302624>.

- [34] Wickramasinghe SR, Stump ED, Grzenia DL, Husson SM, Pellegrino J. Understanding virus filtration membrane performance. *Journal of Membrane Science*. 2010;365(1):160 – 169. Available from: <http://www.sciencedirect.com/science/article/pii/S037673881000699X>.
- [35] Geyer R, Jambeck JR, Law KL. Production, use, and fate of all plastics ever made. *Sci Adv*. 2017 7;3(7):e1700782.
- [36] Haward M. Plastic pollution of the world's seas and oceans as a contemporary challenge in ocean governance. vol. 9. Institute for Marine and Antarctic Studies, University of Tasmania, Hobart, TAS, 7005, Australia. Marcus.Haward@utas.edu.au.; 2018. p. 667.
- [37] Andrady A. *Plastics and Environmental Sustainability*; 2015.
- [38] Ekvall MT, Lundqvist M, Kelpsiene E, Šileikis E, Gunnarsson SB, Cedervall T. Nanoplastics formed during the mechanical breakdown of daily-use polystyrene products. *Nanoscale Adv*. 2019;1:1055–1061. Available from: <http://dx.doi.org/10.1039/C8NA00210J>.
- [39] Lambert S, Wagner M. Formation of microscopic particles during the degradation of different polymers. *Chemosphere*. 2016;161:510 – 517. Available from: <http://www.sciencedirect.com/science/article/pii/S0045653516309390>.
- [40] Revel M, Châtel A, Mouneyrac C. Micro(nano)plastics: A threat to human health? *Current Opinion in Environmental Science And Health*. 2018;1:17 – 23. *Micro and Nanoplastics* Edited by Dr. Teresa A.P. Rocha-Santos. Available from: <http://www.sciencedirect.com/science/article/pii/S2468584417300235>.
- [41] Oceanic N, Administration A. What are microplastics?; 2019 [cited 08/26/2019]. Available from: <https://oceanservice.noaa.gov/facts/microplastics.html>.
- [42] Smith M, Love DC, Rochman CM, Neff RA. Microplastics in Seafood and the Implications for Human Health. *Curr Environ Health Rep*. 2018 Sep;5(3):375–386.

- [43] on Contaminants in the Food Chain (CONTAM) EP. Presence of microplastics and nanoplastics in food, with particular focus on seafood. *EFSA Journal*. 2016;14(6):e04501. Available from: <https://efsa.onlinelibrary.wiley.com/doi/abs/10.2903/j.efsa.2016.4501>.
- [44] Karbalaei S, Hanachi P, Walker TR, Cole M. Occurrence, sources, human health impacts and mitigation of microplastic pollution. *Environ Sci Pollut Res Int*. 2018 Dec;25(36):36046–36063.
- [45] Browne MA, Dissanayake A, Galloway TS, Lowe DM, Thompson RC. Ingested Microscopic Plastic Translocates to the Circulatory System of the Mussel, *Mytilus edulis* (L.). *Environmental Science & Technology*. 2008 07;42(13):5026–5031. Available from: <https://doi.org/10.1021/es800249a>.
- [46] Mato Y, Isobe T, Takada H, Kanehiro H, Ohtake C, Kaminuma T. Plastic resin pellets as a transport medium for toxic chemicals in the marine environment. *Environ Sci Technol*. 2001 1;35(2):318–324.
- [47] Lu Y, Zhang Y, Deng Y, Jiang W, Zhao Y, Geng J, et al. Uptake and Accumulation of Polystyrene Microplastics in Zebrafish (*Danio rerio*) and Toxic Effects in Liver. *Environ Sci Technol*. 2016 4;50(7):4054–4060.
- [48] Eerkes-Medrano D, Leslie HA, Quinn B. Microplastics in drinking water: A review and assessment. *Current Opinion in Environmental Science And Health*. 2019;7:69 – 75. Drinking water contaminants. Available from: <http://www.sciencedirect.com/science/article/pii/S2468584418300436>.
- [49] Kosuth M, Mason SA, Wattenberg EV. Anthropogenic contamination of tap water, beer, and sea salt. *PLoS One*. 2018;13(4):e0194970.
- [50] Salminen A, Hill K, Henry Chung L, James McGrath L, Johnson DG. Protein Separation and Hemocompatibility of Nitride Membranes in Microfluidic Filtration Systems. *Conf Proc IEEE Eng Med Biol Soc*. 2018 7;2018:5814–5817.
- [51] Yuen PK, Goral VN. Low-cost rapid prototyping of flexible microfluidic devices using a desktop digital craft cutter. *Lab Chip*. 2010 2;10(3):384–387.

- [52] Li Z, Zydney AL. Effect of zinc chloride and PEG concentrations on the critical flux during tangential flow microfiltration of BSA precipitates. *Biotechnology Progress*. 2017;33(6):1561–1567. Available from: <https://aiche.onlinelibrary.wiley.com/doi/abs/10.1002/btpr.2545>.
- [53] HO CC, ZYDNEY AL. Theoretical Analysis of the Effect of Membrane Morphology on Fouling during Microfiltration. *Separation Science and Technology*. 1999;34(13):2461–2483. Available from: <https://doi.org/10.1081/SS-100100785>.
- [54] Kelly ST, Opong WS, Zydney AL. The influence of protein aggregates on the fouling of microfiltration membranes during stirred cell filtration. *Journal of Membrane Science*. 1993;80(1):175 – 187. Available from: <http://www.sciencedirect.com/science/article/pii/037673889385142J>.
- [55] Chan R, Chen V. The effects of electrolyte concentration and pH on protein aggregation and deposition: critical flux and constant flux membrane filtration. *Journal of Membrane Science*. 2001;185(2):177 – 192. Available from: <http://www.sciencedirect.com/science/article/pii/S0376738800006451>.
- [56] Dagan Z, Weinbaum S, Pfeffer R. An infinite-series solution for the creeping motion through an orifice of finite length. *Journal of Fluid Mechanics*. 1982;115:505–523.
- [57] Gaborski TR, Snyder JL, Striemer CC, Fang DZ, Hoffman M, Fauchet PM, et al. High-Performance Separation of Nanoparticles with Ultrathin Porous Nanocrystalline Silicon Membranes. *ACS Nano*. 2010 11;4(11):6973–6981. Available from: <https://doi.org/10.1021/nn102064c>.
- [58] Grein TA, Michalsky R, Czermak P. In: Pörtner R, editor. *Virus Separation Using Membranes*. Totowa, NJ: Humana Press; 2014. p. 459–491. Available from: https://doi.org/10.1007/978-1-62703-733-4_26.
- [59] Chung HH, Chan CK, Khire TS, Marsh GA, Clark AJ, Waugh RE, et al. Highly permeable silicon membranes for shear free chemotaxis and rapid cell labeling. *Lab Chip*. 2014 7;14(14):2456–2468.
- [60] 5 Human Albumin. *Transfus Med Hemother*. 2009;36(6):399–407.

-
- [61] Younas H, Zhou Y, Li X, Li X, Sun Q, Cui Z, et al. Fabrication of high flux and fouling resistant membrane: A unique hydrophilic blend of polyvinylidene fluoride/polyethylene glycol/polymethyl methacrylate. *Polymer*. 2019;179:121593. Available from: <http://www.sciencedirect.com/science/article/pii/S0032386119305774>.